Journal of Mathematical Biology manuscript No.
(will be inserted by the editor)

R Thul · G D Smith · S Coombes

A bidomain threshold model of propagating calcium waves

July 26, 2007

Abstract We present a bidomain fire-diffuse-fire model that facilitates mathematical analysis of propagating waves of elevated intracellular calcium (Ca^{2+}) in living cells. Modelling Ca^{2+} release as a threshold process allows the explicit construction of travelling wave solutions to probe the dependence of Ca^{2+} wave speed on physiologically important parameters such as the threshold for Ca^{2+} release from the endoplasmic reticulum (ER) to the cytosol, the rate of Ca^{2+} resequestration from the cytosol to the ER, and the total [Ca^{2+}] (cytosolic plus ER). Interestingly, linear stability analysis of the bidomain fire-diffuse-fire model predicts the onset of dynamic wave instabilities leading to the emergence of Ca^{2+} waves that propagate in a back-and-forth manner. Numerical simulations are used to confirm the presence of these so-called 'tango waves' and the dependence of Ca^{2+} wave speed on the total [Ca^{2+}].

Keywords bidomain models · calcium waves · stability · wave bifurcation

1 Introduction

Calcium ions (Ca^{2+}) are an important second messenger in living cells (1). The diverse physiological roles of intracellular Ca^{2+} signals range from the activation of egg cells at fertilization (2; 3) to the coupling of plasma membrane excitation to cardiac muscle cell contraction (4). While Ca^{2+} influx via voltage-gated Ca^{2+} channels of the plasma membrane can lead to increases in intracellular [Ca^{2+}], another important source is the endoplasmic reticulum (ER), a continuous membrane-delimited intracellular compartment with integrative and regenerative properties analogous to the membranes of electrically excitable cells (5; 6; 7; 8). In neurons and many other cell types, activated metabotropic receptors of the plasma membrane stimulate the production of the intracellular messenger inositol 1,4,5-trisphosphate (IP_3) (9). IP_3 in turn promotes Ca^{2+} release from intracellular stores by binding and activating IP_3 receptor (IP_3R) channels located on the ER membrane (10). In addition to this IP_3-mediated pathway, a second parallel mechanism for Ca^{2+} release is mediated by ryanodine

R Thul · S Coombes
Department of Mathematical Sciences, University of Nottingham, Nottingham, NG7 2RD, UK.
E-mail: ruediger.thul@nottingham.ac.uk
E-mail: stephen.coombes@nottingham.ac.uk

G D Smith
Department of Applied Science, The College of William and Mary, Williamsburg, Virginia 23187, USA.
E-mail: greg@as.wm.edu

receptors (RyRs)—intracellular Ca^{2+} channels on the ER or sarcoplasmic reticulum (SR) that are activated by cyclic ADP ribose (11). Importantly, both IP_3Rs and RyRs can be activated and/or inactivated by intracellular Ca^{2+}leading to ER 'Ca^{2+} excitability' (6; 12). This Ca^{2+} excitability is the physiological basis for IP_3- and Ca^{2+}-induced Ca^{2+} release (IICR and CICR) in excitable and non-excitable cells.

Propagating waves of elevated intracellular [Ca^{2+}] have been characterized in the immature *Xenopus laevis* oocyte (13), mature eggs from a variety of species (14; 15; 16; 17), Ca^{2+}-overloaded cardiac myocytes (18), vascular smooth muscle (19), and many other cell types (20; 21; 22; 23). In many cases intracellular Ca^{2+} waves are primarily due to Ca^{2+} release from internal stores, that is, they can occur in the absence of influx of Ca^{2+} across the plasma membrane. Extensive theoretical work has been carried out in an effort to understand the biophysical mechanisms underlying such waves. In the case of the *Xenopus laevis* oocyte and mature eggs, the focus has been on continuum reaction-diffusion equations in which the release mechanism is modeled in a deterministic fashion (24; 25; 26; 27; 28; 29; 30; 31; 32; 33; 34). For example, in situations where plasma membrane fluxes can be neglected, a one-dimensional continuum model of propagating plane waves of elevated intracellular Ca^{2+} might take the form,

$$\frac{\partial c}{\partial t} = D\frac{\partial^2 c}{\partial x^2} + J_{\rm rel}(c, w, c_{\rm er}) - J_{\rm pump}(c)\,, \tag{1a}$$

$$\frac{\partial w}{\partial t} = \frac{w_\infty(c) - w}{\tau_w(c)}\,, \tag{1b}$$

$$\frac{\partial c_{\rm er}}{\partial t} = D_{\rm er}\frac{\partial^2 c_{\rm er}}{\partial x^2} - \gamma^{-1}\left[J_{\rm rel}(c, w, c_{\rm er}) - J_{\rm pump}(c)\right]\,, \tag{1c}$$

where the cytosolic and ER [Ca^{2+}] given by $c(x,t)$ and $c_{\rm er}(x,t)$ are both functions of space and time, and the release and reuptake fluxes, $J_{\rm rel}(c, w, c_{\rm er})$ and $J_{\rm pump}(c)$, are functions of these two concentrations. In such models the Ca^{2+} release flux is also a function of a Hodgkin-Huxley-like gating variable (w) that represents the fast Ca^{2+}-activation and slower Ca^{2+}-inactivation of a large number of identical IP_3Rs at fixed [IP_3] (35; 36). Note that in (1) the ER is represented as a contiguous compartment with volume fraction γ that is uniformly distributed throughout the cytosol. Spatial whole cell models in which the cytosolic and ER [Ca^{2+}] coexist in this manner are often referred to as 'bidomain' models (37; 38).

The spatial whole cell modelling approach outlined in (1) has suggested or reproduced various distinct modes of transmission of propagating Ca^{2+} waves (38): firstly, solitary and spiral waves that occur when the physiological state of the cytoplasm is excitable (25; 29); secondly, repetitive wave trains and spiral waves that occur when the cytoplasm is oscillatory (28; 29; 30); and thirdly, travelling fronts or 'tides' that occur when the cytoplasm is bistable (31; 39). The first two of these mechanisms have been proposed to be responsible for Ca^{2+} waves observed in the immature *Xenopus laevis* oocyte, while the third mechanism seems to describe the fertilization Ca^{2+} wave in the mature *Xenopus* egg. Interestingly, when the local dynamics of Ca^{2+} release and reuptake are spatially heterogeneous, one-dimensional continuum models (1) are also able to produce a fourth wave phenomenon in which fronts of elevated intracellular [Ca^{2+}] propagate in a back-and-forth manner that resembles the movement of tango dancers (40) and is reminiscent of the behavior of Ca^{2+} waves in nemertean worm (41) and ascidian eggs (42). While spatial heterogeneity of model parameters may give rise to these so-called 'tango waves', the phenomenon can also be observed in models with spatially homogeneous parameters as long as the initial concentration profiles are chosen so that an auxilary variable known as the total [Ca^{2+}] given by

$$c_{\rm T} = c + \gamma c_{\rm er}\,, \tag{2}$$

and satisfying

$$\frac{\partial c_{\rm T}}{\partial t} = D\frac{\partial^2 c}{\partial x^2} + \gamma D_{\rm er}\frac{\partial^2 c_{\rm er}}{\partial x^2}\,, \tag{3}$$

results in a spatially localized bistable domain (40; 43).

One important spatial inhomogeneity known to have a profound impact on propagating IP_3-mediated Ca^{2+} waves is the distribution of IP_3Rs. In the immature *Xenopus* oocyte, for example, IP_3Rs occur in clusters of 10-100 with inter-cluster spacing on the order of a few microns (8). Localized Ca^{2+} elevations due to the activation of an individual IP_3-sensitive Ca^{2+} release sites are referred to as 'Ca^{2+} puffs' (44; 45) and under some conditions this organization of Ca^{2+} release sites reveals itself in cauliflower-like wave fronts (46). Similarly, in cardiac myocytes localized Ca^{2+} elevations due to intracellular Ca^{2+} release mediated by clusters of RyRs known as Ca^{2+} sparks (47) can merge to form Ca^{2+} waves that propagate in a saltatory manner (18).

Although it is possible to modify (1) to include a spatially periodic maximum conductance for Ca^{2+} release (48), a more tractable class of 'fire-diffuse-fire' (FDF) models introduced in (49; 50; 51; 52) are also appropriate for spark- or puff-mediated Ca^{2+} waves. FDF models do not include gating variables for the activation and inactivation of Ca^{2+}-regulated intracellular channels, but instead model Ca^{2+} release as a threshold process in which elevated $[Ca^{2+}]$ triggers a prescribed time course of Ca^{2+} release. For example, in (51) the cytosolic $[Ca^{2+}]$ satisfies

$$\frac{\partial c}{\partial t} = D\frac{\partial^2 c}{\partial x^2} + J_{\rm rel}(x,t)\,, \tag{4}$$

and the release flux is given by

$$J_{\rm rel}(x,t) = \sum_i f(t-T_i)\delta(x-x_i)\,, \tag{5}$$

where the source amplitude $f(t)$ upon triggering of Ca^{2+} release is a continuous function that is zero for $t<0$ and positive for $t\geq 0$. In (5) T_i is the time of the first (and only) release event at release site i located at x_i given by

$$T_i = \inf\{t \mid c(x_i,t) \geq c_{\rm th}\}\,. \tag{6}$$

That is, at each site Ca^{2+} release begins when cytosolic $[Ca^{2+}]$ achieves the threshold concentration $c_{\rm th}$. Analytical and simulation based studies using the FDF formalism ((4) and (5)) have illuminated the differences between continuous propagation (as in mature *Xenopus* eggs) and saltatory propagation (as in Ca^{2+}-overloaded cardiac myocytes) and have been further extended to include reuptake fluxes (53), stochastic Ca^{2+} release (54), diffusion in two dimensions (55), and Ca^{2+} release from continuously and uniformly distributed intracellular channels, i.e., channels that are not clustered at Ca^{2+} release sites (52), in which case the release flux is given by

$$J_{\rm rel}(x,t) = f(t-T(x))\,, \tag{7}$$

where the firing times $T(x)$ are a function of spatial position that take the form

$$T(x) = \inf\{t \mid c(x,t) \geq c_{\rm th}\}\,. \tag{8}$$

To date FDF models with spatially punctate ((5) and (6)) or homogeneous ((7) and (8)) Ca^{2+} release have been used to reproduce and mathematically analyze the properties of solitary Ca^{2+} waves, repetitive wave trains, and travelling fronts, as well as their analogues when release is triggered in a stochastic fashion (49; 50; 51; 52; 53; 56; 54; 55).

In spite of these successes, one of the limitations of the FDF models presented up to now is that the dynamics of ER $[Ca^{2+}]$ is not included in the model formulation. A single equation (4) governs the dynamics of cytosolic Ca^{2+}, rather than the more realistic bidomain equations for concentration balance between the cytosol and the ER such as (1a) and (1c). Because in many cell types Ca^{2+} release does lead to significant local depletion of the ER Ca^{2+} stores, the range of applicability of prior work analyzing properties of Ca^{2+} waves using the FDF formalism is unclear. In particular, the analytical tractability of the FDF formalism has not yet been used to address wave phenomena that require spatial heterogeneity of total $[Ca^{2+}]$ (3) to produce spatially localized bistable domains (40; 43).

In order to overcome this limitation of previous FDF models, we have extended the FDF formalism to include concentration balance between the cytosol and ER (Section 2) and subsequently present what is to our knowledge the first mathematical analysis of a bidomain threshold-release model of propagating Ca^{2+} waves. For clarity, this analysis is developed in two stages. In Section 3 we focus on single domain equations (4) with a release term that is proportional to the concentration difference between the elevated cytosolic [Ca^{2+}] and a fixed ER [Ca^{2+}] (i.e., a shunt). By modelling Ca^{2+} release as a threshold process we explicitly construct travelling wave solutions and perform stability analysis to probe how Ca^{2+} wave speed depends on the threshold for Ca^{2+} release and the ER [Ca^{2+}]. In Section 4 we extend this contruction and analysis to bidomain equations that include time-dependent depletion of the ER [Ca^{2+}], explicitly construct travelling pulse and travelling front solutions, and perform a linear stability analysis that shows the onset of wave instabilities, which lead to the emergence of waves that propagate in a back-and-forth manner (40). Numerical simulations confirm analytical results such as the dependence of wave speed on the total [Ca^{2+}] far from the wave front as well as the presence of so-called tango waves.

2 The Bidomain Fire-Diffuse-Fire Model

For clarity, we restrict our analysis and numerical simulation of the bidomain FDF model to the case where intracellular channels are continuously and uniformly distributed. With this assumption, the bidomain FDF model of propagating Ca^{2+} waves takes the form,

$$\frac{\partial c}{\partial t} = D\frac{\partial^2 c}{\partial x^2} + J_{\rm rel}(c, c_{\rm er}) - J_{\rm pump}(c, c_{\rm er})\,, \tag{9a}$$

$$\frac{\partial c_{\rm er}}{\partial t} = D_{\rm er}\frac{\partial^2 c_{\rm er}}{\partial x^2} - \gamma^{-1}[J_{\rm rel}(c, c_{\rm er}) - J_{\rm pump}(c, c_{\rm er})]\,, \tag{9b}$$

where the release and reuptake fluxes, $J_{\rm rel}(c, c_{\rm er})$ and $J_{\rm pump}(c, c_{\rm er})$, are functions of both the cytosolic and ER [Ca^{2+}], and γ is the effective volume fraction of the ER. When written in the most general form that allows for multiple release events from the same spatial location, the release flux in the bidomain FDF model is given by

$$J_{\rm rel}(x,t) = (c_{\rm er}(x,t) - c(x,t))\sum_m \eta(t - T^m(x))\,, \tag{10}$$

where the release rate $\eta(t) = 0$ for $t < 0$ and $\eta(t) \geq 0$ for $t \geq 0$. The release times $T^m(x)$ are determined by a threshold process such that

$$T^m(x) = \inf\{t \mid c(x,t) \geq c_{\rm th},\ t > T^{m-1}(x) + \tau_R\}\,, \qquad m = 0, 1, \cdots\,, \tag{11}$$

where τ_R is the absolute refractory period for Ca^{2+} release. For simplicity we assume $T^0(x) < -\tau_R$, that is, the absolute refractory period does not influence the time of first release, $T^1(x)$. To complete the bidomain FDF model formulation, the functional form of the reuptake flux is chosen to be

$$J_{\rm pump}(c, c_{\rm er}) = \frac{c}{\tau} - \frac{c_{\rm er}}{\tau_{\rm er}}, \tag{12}$$

a function that is linear in both the cytosolic and ER [Ca^{2+}]. This linear bidirectional reuptake flux (12) is equivalent to the low-affinity limit ($c \ll \kappa$ and $c_{\rm er} \ll \kappa_{\rm er}$) of a previously published bidirectional SERCA pump model (57),

$$J_{\rm pump}(c, c_{\rm er}) = \nu\frac{(c/\kappa)^n - (c_{\rm er}/\kappa_{\rm er})^{n_{\rm er}}}{1 + (c/\kappa)^n + (c_{\rm er}/\kappa_{\rm er})^{n_{\rm er}}}\,, \tag{13}$$

when the Ca^{2+}-binding is not cooperative ($n = n_{\rm er} = 1$) and the time constants in (12) are given by $\tau = \kappa/\nu$ and $\tau_{\rm er} = \kappa_{\rm er}/\nu$.

3 Analysis of the Fire-Diffuse-Fire Model with Shunt

As a first step in our analysis of the bidomain FDF model (9), we consider the associated single domain equations obtained by assuming that the ER $[Ca^{2+}]$ is fixed, i.e., we drop (9b) and consider c_{er} to be a model parameter. This single domain FDF model is applicable when the ER-to-cytosol volume ratio and the diffusion constant within the ER are both large ($\gamma \to \infty$ and $D_{er} \to \infty$). Although an approximation of the full bidomain equations, this single domain model with fixed c_{er} includes the driving force for Ca^{2+} liberation, $c_{er} - c(x,t)$, which decreases upon elevation of intracellular Ca^{2+}. This dynamic driving force or 'shunt' for Ca^{2+} release is potentially important when intracellular Ca^{2+} liberation is triggered by cytosolic $[Ca^{2+}]$ crossing a threshold, but it has been absent from previously published FDF models, which have instead assumed a time-dependent source amplitude (5) or density (7) that is not influenced by cytosolic Ca^{2+} once release is triggered.

3.1 Speed of travelling pulse — arbitrary release shape

We consider a solitary travelling pulse with uniform wave speed v mediated by a single release event at each spatial location and choose a coordinate system such that the cytosolic $[Ca^{2+}]$ crosses the threshold for Ca^{2+} release (c_{th}) at $t = 0$ and $x = 0$. Consequently, release at spatial position x begins at a time given by $T(x) = x/v$. To determine the shape and the velocity of the pulse for a release rate that satisfies $\eta(t) = 0$ for $t < 0$ and $\eta(t) \geq 0$ for $t \geq 0$ but is otherwise arbitrary, it is convenient to work in the co-moving frame. Introducing $\xi = vt - x$ we may re-write the original equation of motion in which c_{er} is a parameter,

$$\frac{\partial c}{\partial t} = D\frac{\partial^2 c}{\partial x^2} - \frac{c}{\tau} + \eta(t - T(x))(c_{er} - c)\,, \tag{14}$$

as $c = c(\xi, t)$ where c satisfies

$$\left(\frac{\partial}{\partial t} + v\frac{\partial}{\partial \xi}\right) c = D\frac{\partial^2 c}{\partial \xi^2} - \frac{c}{\tau} + \eta(\xi/v)(c_{er} - c)\,, \tag{15}$$

and we have used $\eta(t - T(x)) = \eta(t - x/v) = \eta(\xi/v)$. Setting $\partial c/\partial t = 0$ in (15) we find that a stationary profile $c(\xi, t) = c(\xi)$ in the co-moving frame satisfies the ordinary differential equation

$$(\mathrm{d}_\xi - m_+(\xi))(\mathrm{d}_\xi - m_-(\xi))c = F(\xi)\,, \tag{16}$$

where

$$F(\xi) = -\frac{c_{er}}{D}\eta(\xi/v), \qquad m_\pm(\xi) = \frac{v \pm \sqrt{v^2 + 4\epsilon(\xi)D}}{2D}, \qquad \epsilon(\xi) = \frac{1}{\tau} + \eta(\xi/v)\,. \tag{17}$$

Introducing the auxilary variable $z(\xi)$ defined by

$$z = (\mathrm{d}_\xi - m_-(\xi))c\,, \tag{18}$$

we can integrate $(\mathrm{d}_\xi - m_+(\xi))z = F(\xi)$ to find

$$z(\xi) = G_+(\xi, 0)\left[z(0) + \Theta(\xi)\int_0^\xi G_+(0, \xi')F(\xi')\mathrm{d}\xi'\right], \tag{19}$$

where Θ is the Heaviside function, $\Theta(t) = 1$ for $t \geq 0$ and 0 otherwise, and

$$G_\pm(\xi, \xi') = \exp\left(\int_{\xi'}^{\xi} \mathrm{d}s\, m_\pm(s)\right). \tag{20}$$

For $z(\xi)$ to be bounded as $\xi \to \infty$ (long after release begins) we require

$$z(0) = -\int_0^\infty G_+(0, \xi')F(\xi')\mathrm{d}\xi'. \tag{21}$$

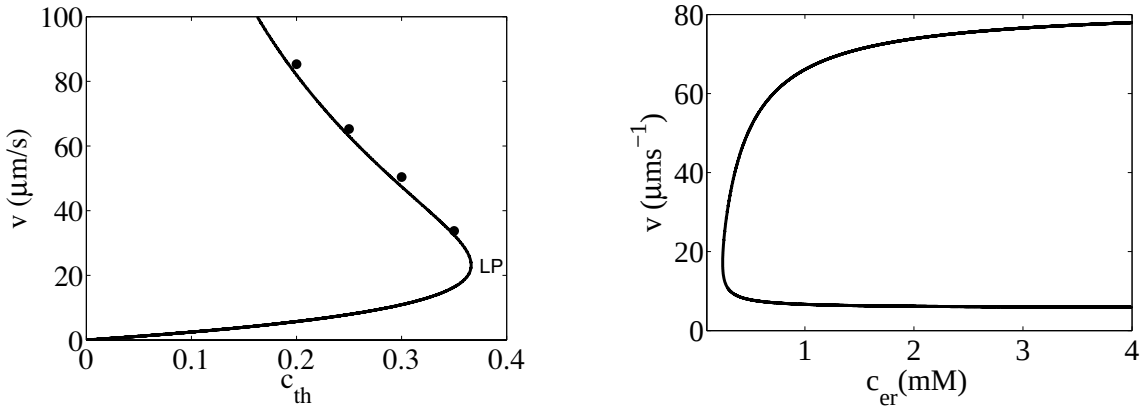

Fig. 1 Speed of a solitary wave as given by (25) with $\eta(t) = \overline{\eta}\Theta(t)\Theta(\Delta - t)$. Filled circles denote results from numerical simulations. Left: $v = v(c_{\rm th})$, with $D = 30\ \mu{\rm m}^2{\rm s}^{-1}$, $c_{\rm er} = 100\ \mu$M, $\Delta = 0.05$ s, $\tau = 0.01\ {\rm s}^{-1}$ and $\overline{\eta} = 1\ {\rm s}^{-1}$. Right: $v = v(c_{\rm er})$ with $D = 30\ \mu{\rm m}^2{\rm s}^{-1}$, $c_{\rm th} = 0.2\ \mu$M, $\Delta = 0.05$ s, $\tau = 0.01\ {\rm s}^{-1}$ and $\overline{\eta}c_{\rm er} = 100\ \mu{\rm M}\ {\rm s}^{-1}$. Of the two branches of solutions, the slower is always unstable.

Next, we integrate (18) to obtain the solution $c(\xi)$ corresponding to $z(\xi)$ in (19),

$$c(\xi) = G_-(\xi, 0)\left[c_{\rm th} + \int_0^\xi G_-(0,\xi')z(\xi'){\rm d}\xi'\right], \tag{22}$$

for which we require

$$c_{\rm th} = z(0)\int_{-\infty}^0 G_-(0,\xi')G_+(\xi',0){\rm d}\xi', \tag{23}$$

for $c(\xi)$ to be bounded as $\xi \to -\infty$ (long before release begins). Note that for $\xi < 0$ (prior to the initiation of release), $\eta = 0$ and $\epsilon = 1/\tau$ in (17) and thus $m_\pm(\xi) = k_\pm$ where

$$k_\pm = \frac{v \pm \sqrt{v^2 + 4D/\tau}}{2D}. \tag{24}$$

Hence, we have the elegant result that the speed of the solitary pulse is determined by the equation

$$c_{\rm th} = \frac{z(0)}{k_+ - k_-} = z(0)\left(\frac{D}{\sqrt{v^2 + 4D/\tau}}\right). \tag{25}$$

3.2 Speed of travelling pulse and wave profile — square pulse release shape

For an example application of the above analysis of travelling pulse speed in the FDF model with a shunt, consider the square pulse release rate with amplitude $\overline{\eta}$ and duration Δ given by $\eta(t) = \overline{\eta}\Theta(t)\Theta(\Delta - t)$. In this case $z(0)$ is easily found from (21) to be

$$z(0) = \frac{\overline{\eta}c_{\rm er}}{Dm_+}\left(1 - {\rm e}^{-m_+ v\Delta}\right), \qquad \text{where} \qquad m_+ = \frac{v + \sqrt{v^2 + 4(\tau^{-1} + \overline{\eta})D}}{2D}. \tag{26}$$

For sufficiently small $c_{\rm th}/c_{\rm er}$ there are two wave speeds that solve (25) and (26). This is illustrated in Figure 1 (left) by varying the threshold for release with fixed ER concentration ($c_{\rm er} = 100\ \mu$M) and pulse duration ($\Delta = 0.05$ s). Note that Figure 1 (left) is qualitatively similar to the $v = v(c_{\rm th})$ plots obtained from FDF models that do not include a shunt (52) and as expected the slower (and lower) branch of solutions is unstable (see Section 3.3). The solid dots in Figure 1 (left) show wave speed calculations obtained from numerical simulations using a finite difference scheme (note agreement with analytical result).

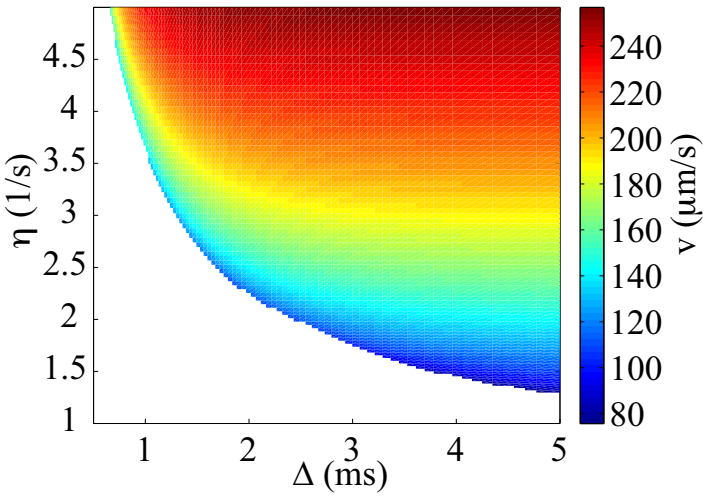

Fig. 2 Pseudocolour plot of the speed v (μm/s) of a stable solitary wave in the $(\Delta, \overline{\eta})$ parameter plane, with $D = 30\ \mu\text{m}^2\text{s}^{-1}$, $c_{\text{er}} = 100\ \mu$M, $c_{\text{th}} = 0.2\ \mu$M, and $\tau = 0.01\ \text{s}^{-1}$.

Figure 1 (right) plots the wave speed as a function of the ER concentration for a fixed threshold for release ($c_{\text{th}} = 0.2\ \mu$M), pulse duration ($\Delta = 0.05$ s), and initial and maximum release amplitude ($\overline{\eta} c_{\text{er}} = 100\ \mu\text{M s}^{-1}$). As expected, we observe that the speed of the stable pulse (upper branch) decreases with decreasing ER $[\text{Ca}^{2+}]$. Note that in the limit $c_{\text{er}} \to \infty$ with fixed $\overline{\eta} c_{\text{er}}$ the shunt model (14) is equivalent to a FDF model with pure source term (7) of the form $f(t) = \overline{\eta} c_{\text{er}} \Theta(t)\Theta(\Delta - t)$. Consequently, the asymptotic stable and unstable wave speeds shown in Figure 1 (right) can be found by taking this limit in (25) and (26) and using the identity $k_+ k_- = -1/(D\tau)$, that is,

$$\frac{c_{\text{th}}}{c_{\text{er}}} = \overline{\eta}\tau \frac{k_-}{k_- - k_+} \left(1 - \text{e}^{-k_+ v \Delta}\right) , \tag{27}$$

a wave speed result first obtained in (52).

A more comprehensive view is presented in Figure 2 that plots the stable wave speed in the $(\Delta, \overline{\eta})$ parameter plane using fixed c_{th} and c_{er}. Note that the minimum wave speed decreases as the release rate during the pulse $\overline{\eta}$ decreases. In the limit of a brief pulse with fixed amplitude given by $\overline{\eta}\Delta = 1$, the limit $\Delta \to 0$ in (25) and (26) such that $\eta(t) \to \delta(t)$ yields a unique wave speed

$$v = \sqrt{\frac{4D/\tau}{(c_{\text{er}}/c_{\text{th}})^2 - 1}} , \qquad \text{when} \qquad c_{\text{er}}/c_{\text{th}} > 1 . \tag{28}$$

The corresponding wave profile is simply $c(\xi) = c_{\text{th}}[\text{e}^{k_- \xi}\Theta(\xi) + \text{e}^{k_+ \xi}\Theta(-\xi)]$, though using the techniques we develop in the next section it can be shown to be unstable.

Figure 3 shows three wave profiles of the FDF model with shunt calculated from (22) using a square-pulse release rate, $\eta(t) = \overline{\eta}\Theta(t)\Theta(\Delta - t)$, and parameters as in Figure 1 (left). The wave profiles shown in the left and right panels of Figure 3 both employ $c_{\text{th}} = 0.2\ \mu$M and correspond to the upper ($v = 81.98\ \mu$m/s) and lower ($v = 5.71\ \mu$m/s) branches of Figure 1, respectively, while the wave profile shown in the middle of Figure 3 corresponds to the limit point in Figure 1 ($c_{\text{th}} = 0.366\ \mu$M and $v = 23.16\ \mu$m/s). When two wave profiles exist for fixed c_{th}, the more slowly propagating wave has a smaller pulse width than the more quickly propagating pulse. In the following section we show that the slower solution branch in Figure 3 (right) is always unstable.

The three wave profiles presented in Figure 3 are nearly identical to profiles obtained from numerical simulations using a finite different scheme (not shown).

3.3 Stability of travelling pulse — arbitrary release shape

For the purposes of a linear stability analysis it is more convenient to work in terms of the original variables (x,t) rather than in the co-moving frame. Our analysis begins by noting that for known release times $T(x)$ the solution to the FDF model with shunt (14) is

$$c(x,t) = \int_{-\infty}^{t} \mathrm{d}s \int_{-\infty}^{\infty} \mathrm{d}y G(x-y, t-s)(c_{\mathrm{er}} - c(y,s))\eta(s - T(y))\,, \tag{29}$$

where $G(x,t)$ is the time-translation invariant Green's function

$$G(x,t) = \frac{1}{\sqrt{4\pi D t}} \mathrm{e}^{-t/\tau} \mathrm{e}^{-x^2/(4Dt)} \Theta(t)\,. \tag{30}$$

As discussed in Section 3.1, we assume $c(x,t)$ is a solitary wave solution mediated by a single release event at each spatial location with $T(x) = x/v$ and $c(x, T(x)) = c_{\mathrm{th}}$. Consequently, $c(x,t) = c(vt - x) = c(v[t - T(x)])$ with $c(\xi)$ given by (22).

Following (52) we consider local perturbations of the release times given by $\widetilde{T}(x) = T(x) + g(x)$ with $g(x) = \phi(x)$ for $x \leq 0$ and $\phi(x)$ a prescribed, bounded function on $(-\infty, 0]$. Asymptotic stability then corresponds to the condition $g(x) \to 0$ as $x \to \infty$ for arbitrary non-uniform initial data $\phi(x)$. The perturbed trajectory $\widetilde{c}(x,t)$ is obtained from (29) under the replacement of $T(x)$ by $\widetilde{T}(x)$. To compute the perturbed trajectory to first order, we make the natural assumption that the perturbed trajectory can be approximated by a time-translation of the unperturbed trajectory so that we may write $\widetilde{c}(x,t) \approx c(x, t - g(x))$. Evaluating $\widetilde{c}(x, \widetilde{T}(x))$ under this assumption from equation (29) and using $\widetilde{c}(x, \widetilde{T}(x)) = c_{\mathrm{th}} = c(x, T(x))$ leads to the condition

$$\int_{-\infty}^{x/v} \mathrm{d}s \int_{-\infty}^{\infty} \mathrm{d}y G(x-y, x/v - s) I'(s - y/v)[g(x) - g(y)] = 0\,, \tag{31}$$

where $I(\xi) = (c_{\mathrm{er}} - c(v\xi))\eta(\xi)$ is the release flux and the prime denotes differentiation, $I'(\xi) = dI/d\xi$. The stability of solutions is then determined by equation (31). More specifically, we now consider perturbations of the firing times of the form $g(x) = \mathrm{e}^{\lambda x}$ to obtain the characteristic equation

$$\mathcal{E}(\lambda) = \mathcal{H}(\lambda) - \mathcal{H}(0) = 0\,, \tag{32}$$

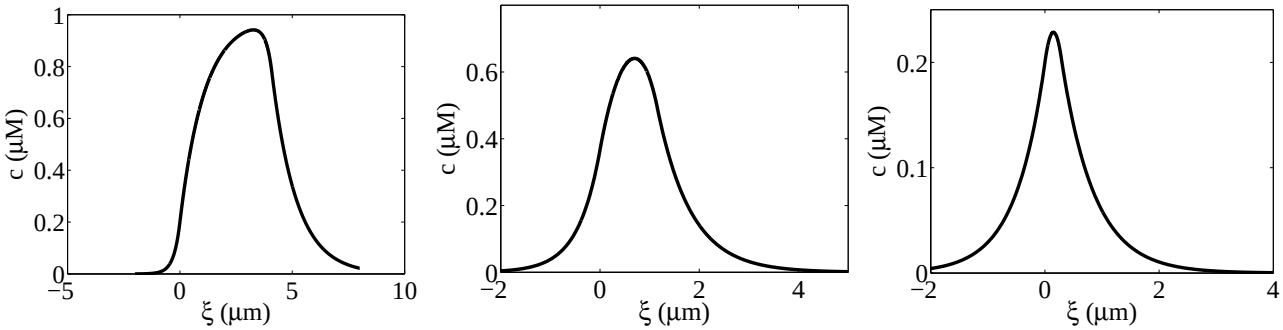

Fig. 3 Three wave profiles corresponding to data on upper branch of Figure 1 (left) at $c_{\mathrm{th}} = 0.2$ μM ($v = 81.98$ $\mu m/s$, stable), the limit point at $c_{\mathrm{th}} = 0.366$ μM ($v = 23.14$ $\mu m/s$, neutrally stable), and the lower branch at $c_{\mathrm{th}} = 0.2$ μM ($v = 5.71$ $\mu m/s$, unstable).

where

$$\mathcal{H}(\lambda) = \int_0^\infty \mathrm{d}s \int_{-\infty}^\infty \mathrm{d}y G(y,s) I'(y/v - s) \mathrm{e}^{-\lambda y} \,. \tag{33}$$

Using the Fourier integral representation

$$G(x,t) = \int_{-\infty}^\infty \frac{\mathrm{d}k}{2\pi} \mathrm{e}^{ikx} \mathrm{e}^{-\sigma(k)t}, \quad \sigma(k) = \frac{1}{\tau} + Dk^2 \,, \tag{34}$$

we may also write (33) in the form

$$\mathcal{H}(\lambda) = \int_{-\infty}^\infty \frac{\mathrm{d}k}{2\pi} \frac{ik\widehat{I}(k)}{\sigma(k/v + i\lambda) + ik} \,, \tag{35}$$

where we introduce the Fourier transform of $I(\xi)$,

$$\widehat{I}(k) = \int_{-\infty}^\infty \mathrm{d}\xi \mathrm{e}^{-ik\xi} I(\xi) \,. \tag{36}$$

Note that going from equation (33) to equation (35) requires $\mathrm{Re}\,\{\sigma(k/v + i\lambda)\} > 0$ for all k. Since a change in stability is indicated by an eigenvalue crossing the imaginary axis, we can restrict our analysis to a region around it where $\lambda = \nu + i\omega$ and $\nu^2 < 1/\tau D$.

Asymptotic stability holds if all non-zero solutions of the characteristic equation (32) have negative real part, while the existence of a solution $\lambda = 0$ reflects the translation invariance of the underlying dynamical system. Equation (35) can be evaluated by closing the contour in the lower-half complex k-plane. Since $I(\xi) = 0$ for $\xi < 0$ it follows that any poles of $\widehat{I}(k)$ lie in the upper-half complex plane and thus we only have to consider poles arising from the zeros of the function $\sigma(k/v + i\lambda) + ik$ (see (52) for a similar calculation). However, when $\lambda \in \mathbb{R}$ we may establish a more general result about branch stability. Because there is always a zero eigenvalue by translation invariance, a real instability occurs when there is a repeated root of the characteristic equation, namely $\mathcal{E}'(0) = 0$. By differentiating the equation defining wave speed $c(x, x/v) = c_{\mathrm{th}}$ with respect to v it is possible to show that

$$\mathcal{E}'(0) = v^2 \frac{\mathrm{d}c_{\mathrm{th}}}{\mathrm{d}v} \,. \tag{37}$$

By contour integration of (35) we find

$$\mathcal{H}(0) = \frac{v^2}{D} \frac{k_+ \widehat{I}(-ivk_+)}{k_+ - k_-} \,, \tag{38}$$

where $k_\pm$ is given by (24) and

$$\widehat{I}(-ivk_+) = \int_{-\infty}^\infty \mathrm{d}\xi \mathrm{e}^{-vk_+\xi} I(\xi) = \int_0^\infty \mathrm{d}\xi \mathrm{e}^{-vk_+\xi} (c_{\mathrm{er}} - c(v\xi)) \eta(\xi) \,. \tag{39}$$

Because the release flux $\eta(c_{\mathrm{er}} - c)$ reverses when $c = c_{\mathrm{er}}$ in the FDF model with shunt, we have that $c(\xi) < c_{\mathrm{er}}$ for travelling wave solutions. Using $c(v\xi) < c_{\mathrm{er}}$ in (38) and (39) we see that $\widehat{I}(-ivk_+) > 0$ and $\mathcal{H}(0) > 0$, and hence $\lim_{\lambda\to\infty} \mathcal{E}(\lambda) = -\mathcal{H}(0) < 0$. Consequently, if $\mathcal{E}'(0) > 0$ there is a positive root of $\mathcal{E}(\lambda)$ that indicates an unstable solution. Thus we find from equation (37) that there is a change of stability at a limit point of a solution branch in the (v, c_{th}) plane. We see that the lower of the two solution branches shown in Figure 1 (left) is unstable to firing perturbations of the form $g(x) = \mathrm{e}^{\lambda x}$ when $\lambda \in \mathbb{R}$.

To determine whether there are dynamic instabilities in the travelling wave solution we must establish whether there are any non-zero solutions for ω of the equation $\mathcal{E}(i\omega) = 0$ along a solution branch. A practical way to explore this spectral problem is to introduce $P(\nu,\omega) = \mathrm{Re}\ \mathcal{E}(\nu + i\omega)$ and $Q(\nu,\omega) = \mathrm{Im}\ \mathcal{E}(\nu + i\omega)$. The zero-contours of P and Q can then be found numerically and plotted in the (ν,ω) plane; where the two contours cross determines a zero of the complex function $\mathcal{E}(\lambda)$ and hence an eigenvalue. Figure 4 uses this approach to show stability functions for the pulse solutions of Figure 3. Notice that upon lowering the velocity, an eigenvalue crosses from the left to the right in the complex plane along the real axis, indicating a change of

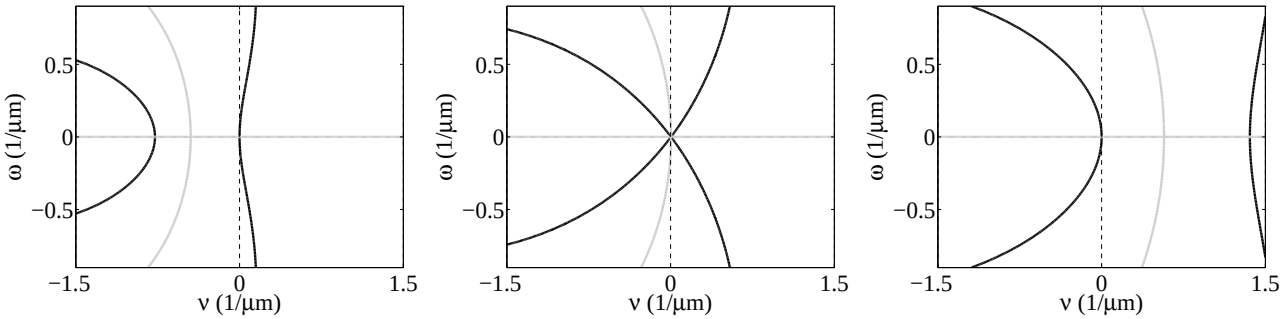

Fig. 4 Three stability functions, corresponding to data on upper branch of Figure 1 (left) at $c_{\rm th} = 0.36$ μM, the limit point and the lower branch at $c_{\rm th} = 0.36$ μM. Solid black lines refer to the zero contour of $\mathrm{Re}\,\mathcal{E}(\lambda)$ and solid grey lines to the zero contour of $\mathrm{Im}\,\mathcal{E}(\lambda)$, respectively.

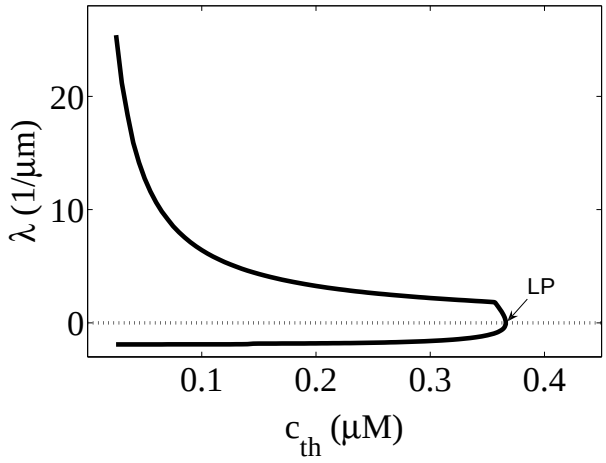

Fig. 5 Critical eigenvalue λ as function of the threshold $c_{\rm th}$ using parameter as in Figure 1 (left). As the branch of solutions in Figure 1 is traversed from the upper to lower branch the critical eigenvalue changes from negative to positive, with a zero at the limit point (LP). Hence, the fast (slow) branch of travelling pulse solutions is stable (unstable).

stability. Figure 5 summarizes this behavior by plotting the real-valued critical eigenvalue λ as a function of the threshold for Ca^{2+} release, $c_{\rm th}$. Note that the eigenvalue changes sign at $c_{\rm th} = 0.366$ μM, which coincides with the limit point in Figure 1 (left) as expected.

4 The bidomain model

While in the previous section we considered a single domain FDF model that included a shunt for Ca^{2+} release, this section focuses on the bidomain FDF model (9) in which the ER $[Ca^{2+}]$ is a dynamic variable, $c_{\rm er}(x,t)$. Our analysis of the bidomain FDF model includes a derivation of an equation for the speed of a travelling pulse or front with arbitrary release shape (Section 4.1), representative travelling and standing waves mediated by square-pulse Ca^{2+} release (Section 4.2), and an analysis of the stability of propagating waves (Section 4.3).

4.1 Speed of travelling pulse — arbitrary release shape

We proceed along the same lines as in Section 3.1 and write the original equations in the co-moving frame. Using $\xi = vt - x$ as above, $(c, c_{\rm er}) = (c(\xi,t), c_{\rm er}(\xi,t))$ satisfies

$$\left(\frac{\partial}{\partial t} + v\frac{\partial}{\partial \xi}\right) c = D\frac{\partial^2 c}{\partial \xi^2} - \left(\frac{c}{\tau} - \frac{c_{\rm er}}{\tau_{\rm er}}\right) + \eta(\xi/v)(c_{\rm er} - c)\,, \tag{40a}$$

$$\left(\frac{\partial}{\partial t} + v\frac{\partial}{\partial \xi}\right) c_{\rm er} = D_{\rm er}\frac{\partial^2 c_{\rm er}}{\partial \xi^2} - \frac{1}{\gamma}\left(\frac{c_{\rm er}}{\tau_{\rm er}} - \frac{c}{\tau}\right) + \frac{1}{\gamma}\eta(\xi/v)(c - c_{\rm er})\,. \tag{40b}$$

A stationary profile $(c(\xi,t), c_{\rm er}(\xi,t)) = (c(\xi), c_{\rm er}(\xi))$ in the co-moving frame satisfies the system of ordinary differential equations $\mathrm{d}_\xi \boldsymbol{x} = A(\xi)\boldsymbol{x}$, where $\boldsymbol{x} = (c, z, c_{\rm er}, z_{\rm er})^T$ and

$$A(\xi) = \begin{bmatrix} m_-(\xi) & 1 & 0 & 0 \\ 0 & m_+(\xi) & \beta(\xi) & 0 \\ 0 & 0 & m_-^{\rm er}(\xi) & 1 \\ \alpha(\xi) & 0 & 0 & m_+^{\rm er}(\xi) \end{bmatrix}, \tag{41}$$

with $m_\pm(\xi)$ given by (17) and $m_\pm^{\rm er}(\xi)$ given by

$$m_\pm^{\rm er}(\xi) = \frac{v \pm \sqrt{v^2 + 4\epsilon_{\rm er}(\xi)D_{\rm er}}}{2D_{\rm er}}\,, \qquad \epsilon_{\rm er}(\xi) = \frac{1}{\gamma}\left(\frac{1}{\tau_{\rm er}} + \eta(\xi/v)\right)\,, \tag{42}$$

and $\alpha(\xi)$ and $\beta(\xi)$ as

$$\alpha(\xi) = -\frac{1}{\gamma D_{\rm er}}\left(\frac{1}{\tau} + \eta(\xi/v)\right)\,, \quad \beta(\xi) = -\frac{1}{D}\left(\frac{1}{\tau_{\rm er}} + \eta(\xi/v)\right)\,. \tag{43}$$

The solution for $\boldsymbol{x}(\xi)$ takes the form $\boldsymbol{x}(\xi) = G(\xi,0)\boldsymbol{x}(0)$ where

$$G(\xi,\xi') = \mathcal{T}\left\{\exp\int_{\xi'}^{\xi} \mathrm{d}s A(s)\right\}\,, \tag{44}$$

and the symbol $\mathcal{T}$ denotes the time-ordering operator, that is,

$$\mathcal{T}[A(\xi)A(\xi')] = A(\xi)A(\xi')\Theta(\xi - \xi') + A(\xi')A(\xi)\Theta(\xi' - \xi)\,. \tag{45}$$

As in Section 3.1 the travelling wave solution is completed by ensuring that solutions are bounded as $\xi \to \pm\infty$ subject to $c(0) = c_{\rm th}$. Note that this construction assumes that the diffusion coefficient for Ca^{2+} in the ER is greater than zero ($D_{\rm er} > 0$) so that (42) is defined. However, travelling pulses with finite velocity can be constructed when $D_{\rm er} = 0$ by deriving a 3×3 analogue of (41) (not shown).

4.2 A conserved quantity in the co-moving frame

The structure of A entails that $\det A = m_+ m_- m_+^{\rm er} m_-^{\rm er} - \alpha\beta = 0$ for all possible release shapes. Consequently, one of the eigenvalues of A is always zero. Denoting this zero eigenvalue as λ_1, we also note that $\lambda_2 + \lambda_3 + \lambda_4 = m_+ + m_- + m_+^{\rm er} + m_-^{\rm er} > 0$ and $\lambda_2\lambda_3\lambda_4 = m_+ m_-(m_+^{\rm er} + m_-^{\rm er}) + m_+^{\rm er} m_-^{\rm er}(m_+ + m_-) < 0$ and, therefore, when the remaining three eigenvalues $(\lambda_2, \lambda_3, \lambda_4)$ are real, two of them are positive and the other is negative.

The physical significance of the zero eigenvalue of A is that a conserved quantity exists in the co-moving frame. In the case of square pulse Ca^{2+} release, $\eta(t) = \overline{\eta}\Theta(t)\Theta(\Delta - t)$, we can explicitly compute its value, because calculating the travelling wave solution from (41–44) simplifies considerably. In this special case, m_+, m_-, $m_+^{\rm er}$, $m_-^{\rm er}$, α and β are all piecewise constant, so that $A(\xi)$ is also piecewise constant. Consequently, we do not have to worry about time ordering. Denoting the right eigenvectors of A and A^T by $\boldsymbol{v}_i$ and $\boldsymbol{u}_i$

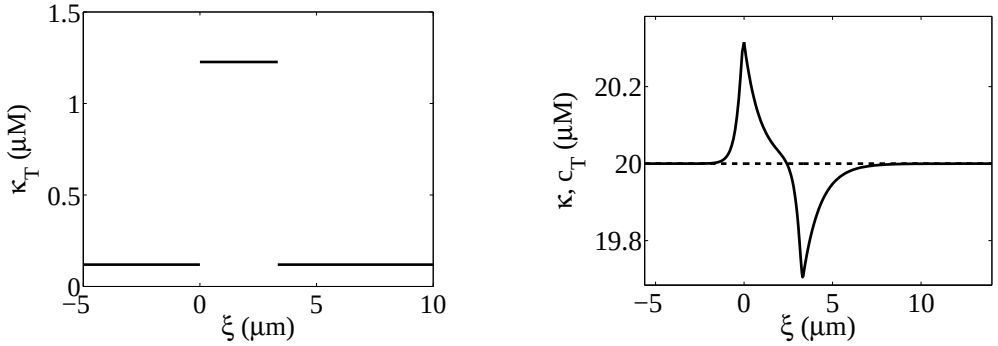

Fig. 6 (Left) The piecewise continuous function $\kappa_T(\xi)$ given by (47). (Right) The total Ca^{2+} concentration in the travelling wave coordinate $c_T(\xi)$ (solid line) is plotted along with the conserved quantity $\kappa(\xi) = c_T^\infty$ (dashed line) given by (49). Parameters: $D = 30\ \mu\text{m}^2\text{s}^{-1}$, $\Delta = 0.05$ s, $\tau = 0.01\ \text{s}^{-1}$, $D_{\text{er}} = 5\ \mu\text{m}^2\text{s}^{-1}$, $\tau_{\text{er}} = 10\ \text{s}^{-1}$, $\bar{\eta} = 1\ \text{s}^{-1}$, $\gamma = 0.167$, $c_{\text{th}} = 0.4\ \mu$M, $c^\infty = 0.119\ \mu$M.

respectively, with corresponding eigenvalues λ_i, we may write $G(\xi) = P\text{e}^{\Lambda\xi}P^{-1}$ where $P = [\boldsymbol{v}_1, \boldsymbol{v}_2, \boldsymbol{v}_3, \boldsymbol{v}_4]$, $P^{-1} = [\boldsymbol{w}_1, \boldsymbol{w}_2, \boldsymbol{w}_3, \boldsymbol{w}_4]^T$, $\boldsymbol{w}_i = \boldsymbol{u}_i/(\boldsymbol{u}_i^T\boldsymbol{v}_i)$ and $\Lambda = \text{diag}[\lambda_1, \lambda_2, \lambda_3, \lambda_4]$. The right eigenvectors $\boldsymbol{v}_i$ and $\boldsymbol{u}_i$ are given explicitly by

$$\boldsymbol{v}_i = \begin{bmatrix} 1 \\ \lambda_i - m_- \\ (\lambda_i - m_+)(\lambda_i - m_-)/\beta \\ \alpha/(\lambda_i - m_+^{\text{er}}) \end{bmatrix}, \qquad \boldsymbol{u}_i = \begin{bmatrix} 1 \\ 1/(\lambda_i - m_+) \\ (\lambda_i - m_+^{\text{er}})(\lambda_i - m_-)/\alpha \\ (\lambda_i - m_-)/\alpha \end{bmatrix}, \tag{46}$$

for $i \in \{1, 2, 3, 4\}$. Because we have set $\lambda_1 = 0$, the conserved quantity can be found by considering the first row of the vector $P^{-1}\boldsymbol{x}$, that is,

$$\kappa_T(\xi) = \frac{1}{\boldsymbol{u}_1^T\boldsymbol{v}_1}\left[c(\xi) - \frac{z(\xi)}{m_+} + \frac{m_+^{\text{er}}m_-}{\alpha}c_{\text{er}}(\xi) - \frac{m_-}{\alpha}z_{\text{er}}(\xi)\right]. \tag{47}$$

This function $\kappa_T(\xi)$ is piecewise constant in the co-moving frame and remains at a fixed level in the ranges of ξ where $A(\xi)$ does not change. By rescaling $\kappa_T(\xi)$ in a piecewise fashion we can construct a quantity $\kappa(\xi)$ that is constant throughout the co-moving frame:

$$\kappa(\xi) = \boldsymbol{u}_1^T\boldsymbol{v}_1\frac{m_+}{m_+ + m_-}\kappa_T(\xi)\,. \tag{48}$$

Using equations (17) and (42) as well as the definitions of z and z_{er}, equation (48) can be written as

$$\kappa(\xi) = \left[1 - \frac{D}{v}\text{d}_\xi\right]c(\xi) + \gamma\left[1 - \frac{D_{\text{er}}}{v}\text{d}_\xi\right]c_{\text{er}}(\xi)\,. \tag{49}$$

For a travelling pulse propagating into a region of the cell where cytosolic and ER $[Ca^{2+}]$ are equilibrated, $\text{d}_\xi c$ and $\text{d}_\xi c_{\text{er}} \to 0$ as $\xi \to -\infty$; similarly, as $\xi \to \infty$ (after the wave passes) the derivative of cytosolic and ER $[Ca^{2+}]$ in the travelling wave coordinate will be zero. By taking these limits in (49) we see that $\kappa(\xi) = c_T^\infty$ where the total (cytosolic plus ER) $[Ca^{2+}]$ far from the pulse is given by $c_T^\infty = \lim_{\xi\to\pm\infty}[c(\xi) + \gamma c_{\text{er}}(\xi)] = c^\infty + \gamma c_{\text{er}}^\infty$. For the solitary travelling pulse solutions shown below, we freely choose c_T^∞ and the parameters of the uptake flux (12), but require $J_{\text{pump}} = 0$ as $\xi \to \pm\infty$ so that $c_{\text{er}}^\infty = c^\infty\tau_{\text{er}}/\tau$ and $c^\infty = c_T^\infty/(1 + \gamma\tau_{\text{er}}/\tau)$.

Figure 6 (left) plots $\kappa_T(\xi)$ for a solitary travelling pulse using a cytosolic $[Ca^{2+}]$ far from the pulse of $c^\infty = 0.119\ \mu$M, which employing reuptake flux time constants of $\tau = 0.01$ s and $\tau_{\text{er}} = 10$ s results in $c_{\text{er}}^\infty = 119.28\mu$M and $c_T^\infty = 20\ \mu$M. The piecewise constant function $\kappa_T(\xi)$ has the same value in the wake as in the front of the pulse due to $c(-\infty) = c(\infty)$ and $c_{\text{er}}(-\infty) = c_{\text{er}}(\infty)$ at a fixed value of c_T^∞. The dotted line in Figure 6 (right)

shows the constant function $\kappa(\xi) = c_T^\infty = 20\ \mu$M. The solid line in Figure 6 (right) shows the total $[Ca^{2+}]$ in the travelling wave coordinate $c_T(\xi)$ asymptotically approaching c_T^∞. Note that $c_T(\xi)$ is elevated near the wave front and depressed near the wave back, consistent with observations in bidomain models with Hodgkin-Huxley-like gating variables (40; 43).

4.3 Square pulse release — speed of travelling pulse and wave profiles

In order to construct travelling wave solutions mediated by square pulse release, we denote the piecewise constant matrix A (41) by A^∞ when $\xi \notin (0, v\Delta)$ and use similar superscripts to label the associated eigenvectors and eigenvalues. It is also convenient to introduce the sets $\mathcal{J}_\pm$ defined by

$$\mathcal{J}_- = \{j \mid \lambda_j \geq 0\}\,, \qquad \mathcal{J}_+ = \{j \mid \lambda_j \leq 0\}\,. \tag{50}$$

In this way we may write a bounded solution as $\boldsymbol{x} = (x_1, x_2, x_3, x_4)^T = (c, z, c_{\rm er}, z_{\rm er})^T$ where

$$x_i(\xi) = \begin{cases} \displaystyle\sum_{j\in\mathcal{J}_-} a_j^- G_{ij}^\infty(\xi)\,, & \xi \leq 0\,, \\ \displaystyle\sum_{j} a_j G_{ij}(\xi)\,, & 0 < \xi < v\Delta\,, \\ \displaystyle\sum_{j\in\mathcal{J}_+} a_j^+ G_{ij}^\infty(\xi)\,, & \xi \geq v\Delta\,, \end{cases} \tag{51}$$

with the still unknown set of coefficients $\{a_j^-, a_j, a_j^+\}$. Note that the components of $G^\infty(\xi)$ are $[P^\infty \mathrm{e}^{\Lambda^\infty \xi}(P^\infty)^{-1}]_{ij}$, where $[\mathrm{e}^{\Lambda^\infty\xi}]_{ij} = \delta_{ij}\mathrm{e}^{\lambda_i^\infty \xi}\Theta(-\lambda_i^\infty\xi)$, $\Lambda^\infty = \mathrm{diag}[\lambda_1^\infty, \lambda_2^\infty, \lambda_3^\infty, \lambda_4^\infty]$, and P^∞ is given by (46) with the substitution of λ_i^∞ for λ_i. To ensure that both $c(\xi)$ and $c_{\rm er}(\xi)$ are C^1 functions we need to match x_i and $\mathrm{d}x_i/\mathrm{d}\xi$ at $\xi = 0$ and $\xi = v\Delta$ for $i = 1, 3$. Introducing $H_{ij} = \mathrm{d}G_{ij}/\mathrm{d}\xi$ and $H_{ij}^\infty = \mathrm{d}G_{ij}^\infty/\mathrm{d}\xi$ the eight matching conditions are

$$\sum_{j\in\mathcal{J}_-} a_j^- G_{ij}^\infty(0) = \sum_j a_j G_{ij}(0)\,, \qquad \sum_j a_j G_{ij}(v\Delta) = \sum_{j\in\mathcal{J}_+} a_j^+ G_{ij}^\infty(v\Delta)\,, \tag{52}$$

$$\sum_{j\in\mathcal{J}_-} a_j^- H_{ij}^\infty(0) = \sum_j a_j H_{ij}(0)\,, \qquad \sum_j a_j H_{ij}(v\Delta) = \sum_{j\in\mathcal{J}_+} a_j^+ H_{ij}^\infty(v\Delta)\,, \tag{53}$$

for $i = 1, 3$. If we demand that $x_1(0) = c(0) = c_{\rm th}$ then we may regard these nine equations as a linear system in nine unknowns (parameterised by v) that may be solved explicitly with, e.g., Cramer's rule. Imposing the known asymptotic value for c_T^∞ determines the unknown wave speed. Hence, in this fashion we obtain both the wave profile, given by equation (51), and the wave speed v, as a function of model parameters.

Figure 7 (left) shows the velocity of solitary pulses exhibited by the bidomain model with square pulse Ca^{2+} release as a function of total $[Ca^{2+}]$ far from the pulse (c_T^∞, left). Recalling the relationship $c_{\rm er}^\infty = (c_T^\infty - c^\infty)/\gamma$ we see the intuitive result that the velocity of the fast wave (solid line, see Section 4.6) is an increasing function of the ER $[Ca^{2+}]$ being invaded by the wave. Figure 7 (right) shows the velocity of stable solitary pulses is a decreasing function of the ER volume fraction (γ) for fixed c_T^∞.

Figures 8 and 9 depict solitary pulse profiles corresponding to Figure 7 (left). Note that the ER $[Ca^{2+}]$ before and after the travelling pulse is reduced in the middle panel of Figures 9 because the total $[Ca^{2+}]$ used is less than that of the left and right panels ($c_T^\infty = 14.67\ \mu$M and 20 μM, respectively).

4.4 Travelling fronts with step release

In the case of release events where activated Ca^{2+} release sites do not close ($\Delta \to \infty$), the release rate takes the form $\eta(t) = \overline{\eta}\Theta(t)$ and the bidomain FDF model exhibits travelling fronts. Travelling fronts with finite

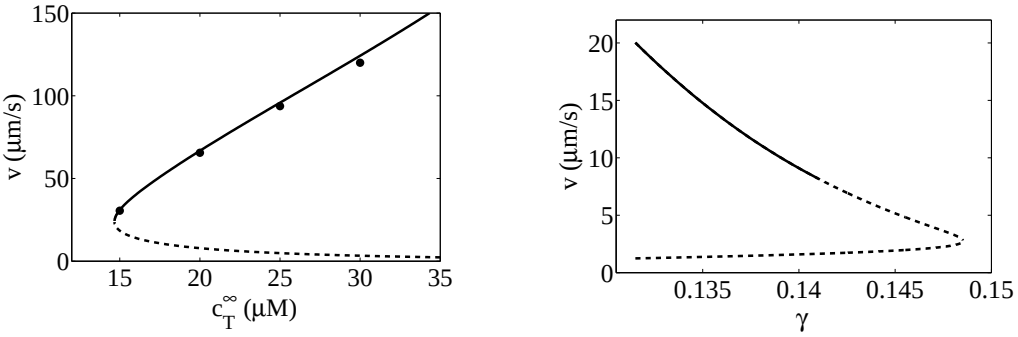

Fig. 7 Speed of a solitary pulse in the bidomain model with square pulse release given by $\eta(t) = \overline{\eta}(c_{\rm er} - c)$ as a function of total $[Ca^{2+}]$ far from the pulse (c_T^∞, left) and the ER volume fraction (γ, right). Solid and dashed lines denote stable and unstable solutions, respectively. Filled circles indicate simulations results using a finite difference numerical scheme. Parameters (left): $\Delta = 0.05$ s, $D_{\rm er} = 5\ \mu{\rm m}^2{\rm s}^{-1}$, $\gamma = 0.167$, $c_{\rm th} = 0.4\ \mu$M, $\tau_{\rm er} = 10\ {\rm s}^{-1}$. Parameters (right): $\Delta = 3$ s, $\tau = 0.01\ {\rm s}^{-1}$, $D_{\rm er} = 2\ \mu{\rm m}^2{\rm s}^{-1}$, $c_T^\infty = 2\ \mu$M, $c_{\rm th} = 0.2\ \mu$M, $\tau_{\rm er} = 1\ {\rm s}^{-1}$. In both panels $D = 30\ \mu{\rm m}^2{\rm s}^{-1}$, $\tau = 0.01\ {\rm s}^{-1}$, $\overline{\eta} = 1\ {\rm s}^{-1}$.

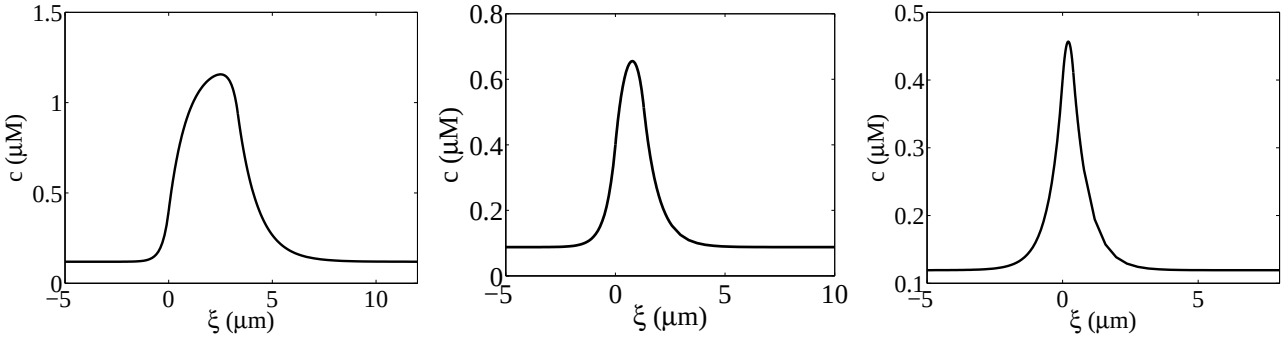

Fig. 8 Three wave profiles corresponding to data on upper branch of Figure 7 (left) at $c_T^\infty = 20\ \mu$M ($v = 66.75\ \mu{\rm m}/s$, stable), the limit point at $c_T^\infty = 14.6712\ \mu$M ($v = 24.3\ \mu{\rm m}/s$, neutrally stable), and the lower branch at $c_T^\infty = 20\ \mu$M ($v = 7.88\ \mu{\rm m}/s$, unstable).

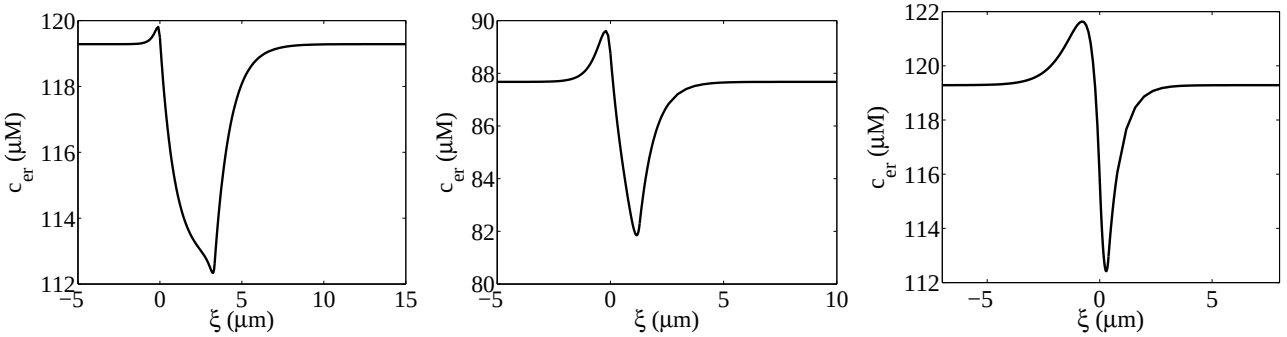

Fig. 9 Three lumenal wave profiles corresponding to the three panels of Figure 8.

velocity and non-zero diffusion coefficient for luminal Ca^{2+} ($D_{\rm er}$) can be constructed in a manner similar to that presented in the previous section. Let $\{b_j^-, b_j^+\}$ denote a set of still unknown coefficients and G_{ij}^∞ be defined as after equation (51), then a front solution is given by

$$x_i(\xi) = \begin{cases} \sum_{j\in\mathcal{J}_-} b_j^- G_{ij}^\infty(\xi)\,, & \xi < 0\,, \\ \sum_{j\in\mathcal{J}_+} b_j^+ G_{ij}(\xi)\,, & \xi \geq 0\,. \end{cases} \tag{54}$$

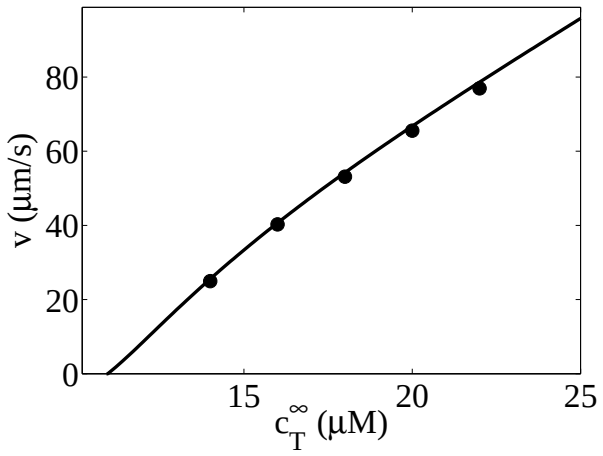

Fig. 10 Solid line shows solitary travelling front velocity in the bidomain FDF model calculated from (54). Filled circles show results from simulations using a finite difference numerical scheme. Parameters: $D = 30\ \mu\mathrm{m}^2\mathrm{s}^{-1}$, $\tau = 0.01\ \mathrm{s}^{-1}$, $D_{\mathrm{er}} = 5\ \mu\mathrm{m}^2\mathrm{s}^{-1}$, $\tau_{\mathrm{er}} = 10\ \mathrm{s}^{-1}$, $\overline{\eta} = 1\ \mathrm{s}^{-1}$, $c_{\mathrm{th}} = 0.4\ \mu\mathrm{M}$ and $\gamma = 0.167$.

In this construction, we require the release (J_{rel}) and reuptake (J_{pump}) fluxes to be balanced far from the wave front so that $[c/\tau - c_{\mathrm{er}}/\tau_{\mathrm{er}}] \to 0$ as $\xi \to -\infty$ and $[c/\tau - c_{\mathrm{er}}/\tau_{\mathrm{er}}] \to \overline{\eta}(c_{\mathrm{er}} - c)$ as $\xi \to \infty$, that is,

$$\left(\frac{1}{\tau} + \eta(\pm\infty)\right) c(\pm\infty) = \left(\frac{1}{\tau_{\mathrm{er}}} + \eta(\pm\infty)\right) c_{\mathrm{er}}(\pm\infty)\,. \tag{55}$$

Thus, while the cytosolic [Ca^{2+}] being invaded by the wave front is a free parameter, $c(\xi = -\infty) = c^\infty$, the ER [$Ca^{2+}$] at $\xi = -\infty$ is constrained by (55) to be $c_{\mathrm{er}}(\xi = -\infty) = \tau_{\mathrm{er}} c^\infty/\tau$ and the total [Ca^{2+}] is thus $c_T^\infty = c^\infty(1 + \gamma\tau_{\mathrm{er}}/\tau)$. Because travelling front solutions will have the same total [Ca^{2+}] after the wave passes (see Section 4.2), we may also write $c(\xi = \infty) + \gamma c_{\mathrm{er}}(\xi = \infty) = c_T^\infty$, which combined with (55) implies

$$c(\xi = \infty) = \frac{\left(\tau_{\mathrm{er}}^{-1} + \overline{\eta}\right)/\gamma}{(\tau^{-1} + \overline{\eta}) + \left(\tau_{\mathrm{er}}^{-1} + \overline{\eta}\right)/\gamma} c_T^\infty\,, \quad c_{\mathrm{er}}(\xi = \infty) = \frac{\left(\tau^{-1} + \overline{\eta}\right)/\gamma}{(\tau^{-1} + \overline{\eta}) + \left(\tau_{\mathrm{er}}^{-1} + \overline{\eta}\right)/\gamma} c_T^\infty\,. \tag{56}$$

Thus, in (54) matching x_i and $\mathrm{d}x_i/\mathrm{d}\xi$ at $\xi = 0$ for $i = 1, 3$ together with a fixed value for c^∞ (or, alternatively, c_T^∞) and $x_1(0) = c(0) = c_{\mathrm{th}}$ determines the profile and the speed of the front.

Figure 10 uses this approach to calculate the travelling front velocity (v) as a function of total [Ca^{2+}] (c_T^∞). Note that when other model parameters are fixed, travelling fronts exist only above a minimal value of total [Ca^{2+}] and v is an increasing function of c_T^∞, a parameter that increases the cytosolic and ER [Ca^{2+}] both before and after release.

4.5 Standing waves with step release

In addition to travelling fronts, the bidomain model also supports standing interfaces between states of high and low [Ca^{2+}] when the Ca^{2+} release rate takes the form $\eta(t) = \overline{\eta}\Theta(t)$. Pinned fronts represent stationary solutions of the model equations as expressed in terms of the physical coordinates (x, t) (9). Writing $\boldsymbol{y} = (c, z, c_{\mathrm{er}}, z_{\mathrm{er}})^T$ we find that for a standing wave pinned at $x = 0$, $\mathrm{d}_x\boldsymbol{y} = B(x)\boldsymbol{y}$, where $B(x)$ has the same structure as $A(\xi)$ in (41), but with the piecewise constant entries given by

$$m_\pm(x) = \pm\sqrt{\frac{1}{D}\left(\frac{1}{\tau} + \eta(x)\right)}\,, \qquad m_\pm^{\mathrm{er}}(x) = \pm\sqrt{\frac{1}{\gamma D_{\mathrm{er}}}\left(\frac{1}{\tau_{\mathrm{er}}} + \eta(x)\right)}\,, \tag{57}$$

and

$$\alpha(x) = -\frac{1}{\gamma D_{\rm er}}\left(\frac{1}{\tau} + \eta(x)\right), \quad \beta(x) = -\frac{1}{D}\left(\frac{1}{\tau_{\rm er}} + \eta(x)\right). \tag{58}$$

Note that each of the above expressions takes two different values as $\eta(x)$ steps from 0 to $\overline{\eta}$ at $x = 0$. It follows that B possesses two zero eigenvalues and two non-zero eigenvalues $\pm\sigma$ where

$$\sigma(x) = -\sqrt{(m_+)^2 + (m_+^{\rm er})^2}\,. \tag{59}$$

While $B(x)$ cannot be diagonalised because there is a one-dimensional eigenspace associated with the repeated zero eigenvalue, it is similar to a Jordan normal form. The matrix $\widetilde{P}$ that contains the generalised eigenvectors of B is given by

$$\widetilde{P} = \begin{bmatrix} 1 & 1 & 0 & 1 \\ \sigma - m_- & -m_- & 1 & -(\sigma + m_-) \\ -\dfrac{D}{D_{\rm er}\gamma} & \dfrac{m_- m_+}{\beta} & 0 & -\dfrac{D}{D_{\rm er}\gamma} \\ \dfrac{\alpha}{\sigma - m_+^{\rm er}} & -\dfrac{\alpha}{m_+^{\rm er}} & -\dfrac{m_+^2}{\beta} & -\dfrac{\alpha}{\sigma + m_+^{\rm er}} \end{bmatrix}, \tag{60}$$

where $(\lambda_1, \lambda_2, \lambda_3, \lambda_4) = (\sigma, 0, 0, -\sigma)$ and we have used equation (46) and the identity $(\sigma - m_+)(\sigma - m_-)/\beta = -D/(D_{\rm er}\gamma)$. A solution for $\boldsymbol{y}$ follows from the transformed system $\mathrm{d}_x\widetilde{\boldsymbol{y}} = \widetilde{\Lambda}\widetilde{\boldsymbol{y}}$ where $\widetilde{\boldsymbol{y}} = \widetilde{P}^{-1}\boldsymbol{y}$ and

$$\widetilde{\Lambda} = \begin{bmatrix} \sigma & 0 & 0 & 0 \\ 0 & 0 & 1 & 0 \\ 0 & 0 & 0 & 0 \\ 0 & 0 & 0 & -\sigma \end{bmatrix}. \tag{61}$$

It is evident from equation (61) that the third component of $\widetilde{\boldsymbol{y}}$ is constant. Employing

$$\widetilde{P}^{-1} = \begin{bmatrix} \dfrac{m_+^2\,(\sigma - m_+)}{2\sigma^3} & \dfrac{m_+^2}{2\sigma^3} & \dfrac{\beta(\sigma - m_+^{\rm er})}{2\sigma^3} & \dfrac{\beta}{2\sigma^3} \\ \dfrac{\left(m_+^{\rm er}\right)^2}{\sigma^2} & 0 & -\dfrac{\beta}{\sigma^2} & 0 \\ \dfrac{\left(m_+^{\rm er}\right)^2 m_-}{\sigma^2} & \dfrac{\left(m_+^{\rm er}\right)^2}{\sigma^2} & \dfrac{\beta m_+^{\rm er}}{\sigma^2} & -\dfrac{\beta}{\sigma^2} \\ \dfrac{m_+^2\,(\sigma + m_+)}{2\sigma^3} & -\dfrac{m_+^2}{2\sigma^3} & \dfrac{\beta(\sigma + m_+^{\rm er})}{2\sigma^3} & -\dfrac{\beta}{2\sigma^3} \end{bmatrix}, \tag{62}$$

we find that $\widetilde{y}_3 = 0$ and, consequently, $\widetilde{y}_2$ is piecewise constant with a step discontinuity at $x = 0$, that is,

$$\widetilde{y}_2(x) = \frac{1}{\sigma^2}\left[\left(m_+^{\rm er}\right)^2 c(x) - \beta c_{\rm er}(x)\right] = \begin{cases} c(-\infty)\,, & x < 0\,, \\ c(+\infty)\,, & x \geq 0\,, \end{cases} \tag{63}$$

where the second equality is determined by evaluating $\widetilde{y}_2$ at $x = \pm\infty$ where the release and reuptake fluxes are assumed to be balanced (55). Note that equation (63) only establishes a relation between $\widetilde{y}_2$ and the cytosolic $[\mathrm{Ca}^{2+}]$ at the boundary, but the latter is still undetermined.

Also note that by multiplying (9b) with γ and then adding the resulting expression to (9a), we see that the stationary solution of (9) satisfies $Dc + \gamma D_{\rm er} c_{\rm er} = ax + b$ where a and b are constants. Assuming no longitudinal fluxes for c and $c_{\rm er}$ far from the pinned wave front we have $a = 0$. The constant b can be related to $c(-\infty)$ by evaluating $Dc + \gamma D_{\rm er} c_{\rm er}$ as $x \to -\infty$ where from (55) we have $c_{\rm er}(-\infty) = c(-\infty)\tau_{\rm er}/\tau$, that is, $b = [D + \gamma D_{\rm er}\tau_{\rm er}/\tau]c(-\infty)$. But b can also be related to $c(\infty)$ by evaluating $Dc + \gamma D_{\rm er} c_{\rm er}$ as $x \to \infty$ where from (55) we have $c_{\rm er}(\infty) = c(\infty)(\tau^{-1} + \overline{\eta})/(\tau_{\rm er}^{-1} + \overline{\eta})$, that is, $b = [D + \gamma D_{\rm er}(\tau^{-1} + \overline{\eta})/(\tau_{\rm er}^{-1} + \overline{\eta})]c(\infty)$. Thus, $c(-\infty)$ and $c(\infty)$ are linearly related through

$$\left[D + \gamma D_{\rm er}\frac{\tau_{\rm er}}{\tau}\right] c(-\infty) = \left[D + \gamma D_{\rm er}\frac{\tau^{-1} + \overline{\eta}}{\tau_{\rm er}^{-1} + \overline{\eta}}\right] c(\infty)\,. \tag{64}$$

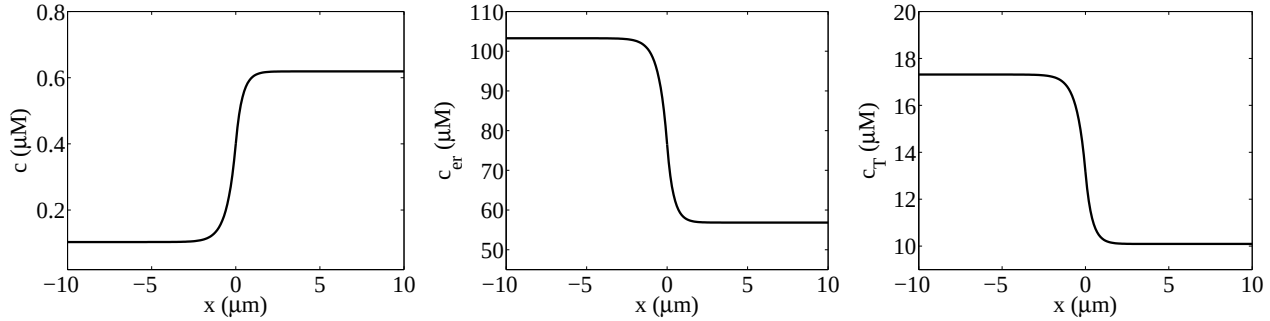

Fig. 11 Front profiles in the cytosol (left) and the lumen (middle) as well as the total Ca^{2+} concentration (right) for a pinned wave. Parameter values as in Figure 10.

Recalling $\boldsymbol{y} = \widetilde{P}\widetilde{\boldsymbol{y}}$, we immediately find that

$$c(x) = \begin{cases} c\,(-\infty) + a^{-}\exp(-\sigma x)\,, & x \leq 0\,, \\ c\,(\infty) + a^{+}\exp(\sigma x)\,, & x > 0\,, \end{cases} \tag{65}$$

with the three unknowns $c(-\infty)$, a^{-} and a^{+} due to equation (64). These three remaining unknowns are determined by demanding that c is C^1 and $c(0) = c_{\mathrm{th}}$. Note that for the standing wave solutions there are two distinct total Ca^{2+} concentrations far from the pinned front, that is, $\lim_{x\to-\infty} c_T(x) \neq \lim_{x\to\infty} c_T(x)$ where $c_T = c + \gamma c_{\mathrm{er}}$. For any given threshold concentration c_{th}, there is exactly one pinned solution of equation (9) for nonzero D_{er}. Figure 11 shows an example for a pinned front that illustrates the different values of the total Ca^{2+} concentration in the front and the wake of the wave.

4.6 Stability of travelling waves

Proceeding along similar lines to Section 3.3 and linearising around a travelling wave solution $(c(\xi), c_{\mathrm{er}}(\xi))$ we find that the characteristic equation (32) has the same form as before under the replacement of $G(x,t)$ by $G_{11}(x,t) - \gamma^{-1}G_{12}(x,t)$ and $I(\xi)$ by $(c_{\mathrm{er}}(v\xi) - c(v\xi))\eta(\xi)$ in equation (33). We refer the reader to the Appendix for details and a definition of $G_{ij}(x,t)$, $i,j = 1,2$.

Figure 12 shows three stability functions for the speed curve depicted in Figure 7 (left). Upon decreasing travelling front velocity v, an eigenvalue crosses to the right hand of the complex plane along the real axis, signalling a change of stability. As with the shunt model, there is always a zero eigenvalue reflecting translational invariance and, consequently, the point of stability exchange is characterised by a repeated zero eigenvalue.

Importantly, the bidomain model also supports dynamic instabilities. For example, Figure 13 shows three stability functions that correspond to the speed curve of Figure 7 (right). When the ER to cytosol volume ratio γ is increased, an eigenvalue crosses the imaginary axis at a non-zero value of $\omega = \mathrm{Im}(\lambda)$. We therefore expect oscillatory perturbations with a frequency ω to grow, leading to solutions with a non-constant profile in the travelling wave frame that periodically vary around the unstable fast wave. This is confirmed in direct numerical simulations, where we see the emergence of 'back-and-forth' waves (like those in Figures 14 and 15). We note that the frequency of oscillations determined from the linear stability analysis is not a strong predictor of the frequencies seen in numerical simulations of the full nonlinear model, suggesting that these wave bifurcations are sub-critical in nature.

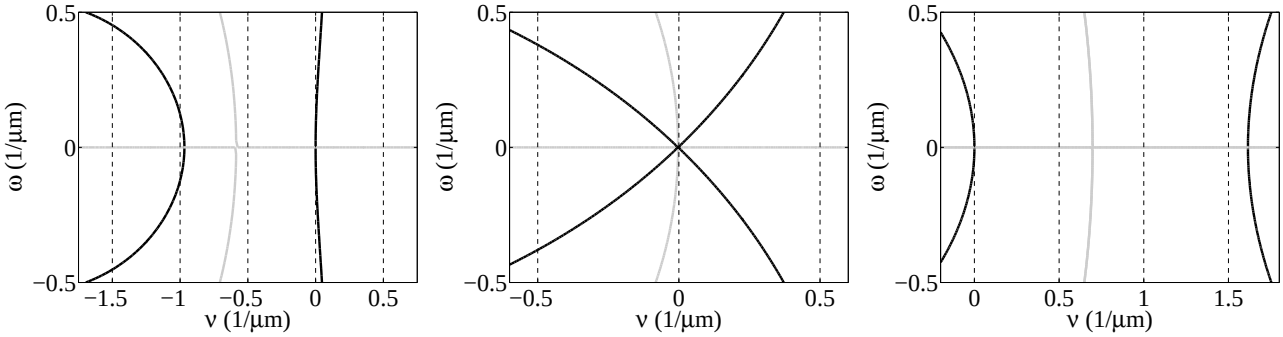

Fig. 12 Stability plots for data on upper branch at $c_T^\infty = 15$ μM (left), the limit point (middle) and the lower branch at $c_T^\infty = 15$ μM (right) of Figure 7 (left). Solid black lines refer to the zero contour of $\mathrm{Re}\,\mathcal{E}(\lambda)$ and solid grey lines to the zero contour of $\mathrm{Im}\,\mathcal{E}(\lambda)$, respectively. Hence, slow pulses in the full bidomain model are unstable.

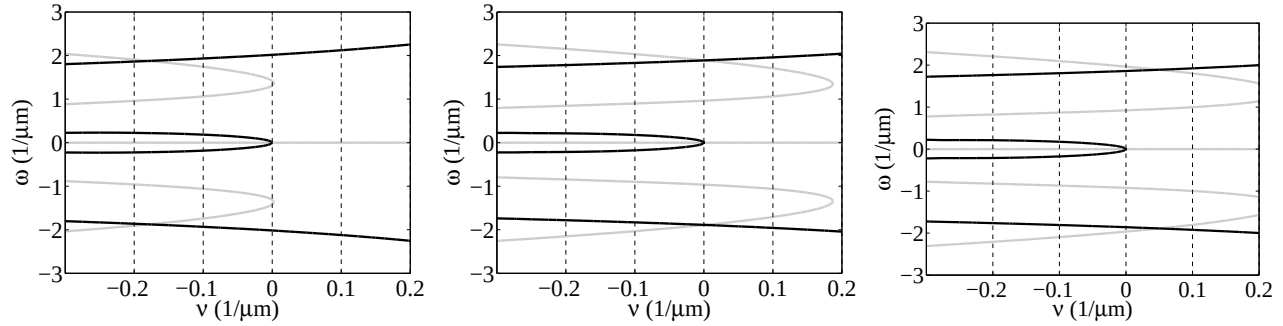

Fig. 13 Dynamic instability illustrated by stability functions that correspond to the upper branch of Figure 7 (right) for $\gamma = 0.1405$ (right), $\gamma_{crit} = 0.14098$ (middle), and $\gamma = 0.1411$ (right). Solid black lines refer to the zero contour of $\mathrm{Re}\,\mathcal{E}(\lambda)$ and solid grey lines to the zero contour of $\mathrm{Im}\,\mathcal{E}(\lambda)$, respectively. Hence, fast pulses in the full bidomain model may undergo dynamic instabilities (since a pair of eigenvalues may cross through the imaginary axis).

4.7 Numerical simulations of tango waves

As mentioned above, many of the analytical results obtained here have been validated against simulations that integrate (9) using a finite difference numerical scheme. For example, the filled circles in Figures 7 and 10 show numerically calculated wave speeds that closely follow the analytical results (solid lines). Moreover, perturbations of front and pulse solutions that are predicted to be linearly stable were found to decay in numerical simulations, thereby supporting the results of Section 4.6 (not shown).

Interestingly, Figures 14 and 15 show complex cytosolic profiles that result when the same perturbations are applied to the bidomain FDF model with parameters chosen near a point of dynamical instability. In contrast to pulse and front solutions that travel with a constant speed in one direction, in these cases we observe waves that propagate in a back-and-forth manner and are reminiscent of a dynamical phenomenon first reported in (40) and dubbed 'tango waves'.

Using release duration of $\Delta = 3$ s and refractory period of $\tau_R = 0.5$ s, Figure 14 (left) resembles earlier findings, especially with respect to the wave form and to the emergence of additional pulses. Whenever a tango wave reverses its direction after invading the low $[Ca^{2+}]$ region, travelling pulses are released that travel to the right with constant speed. While the first four tango waves initiate only one pulse, the following three tango waves give rise to two pulses each. Figure 14 (right) shows the form of the tango wave changing appreciably when the ER to cytosol volume fraction γ is increased from 0.138 to 0.160 and the refractory period is set to

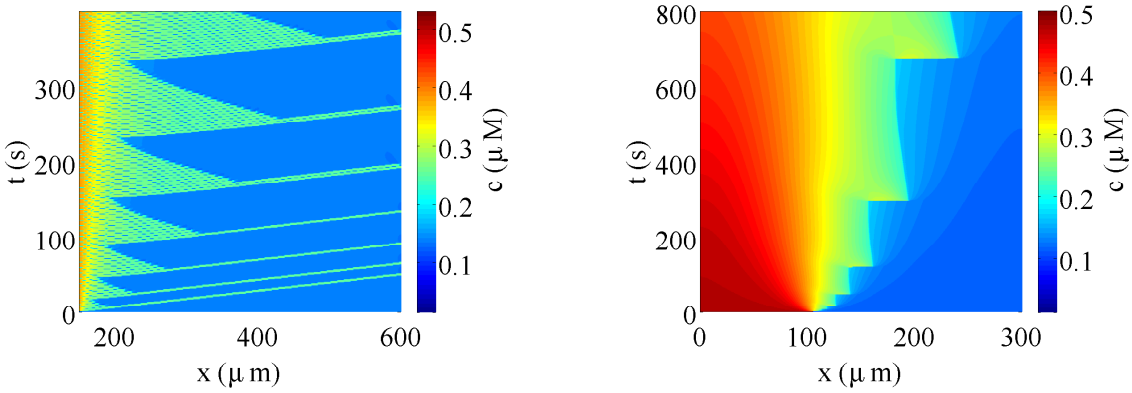

Fig. 14 Tango waves in the vicinity of the point of instability shown in the right panel of Figure 7. Parameters as previous figure with $\tau_R = 0.5$ s (left) and $\tau_R = 0$ s (right). The pseudocolour plot shows $c(x,t)$ in μM.

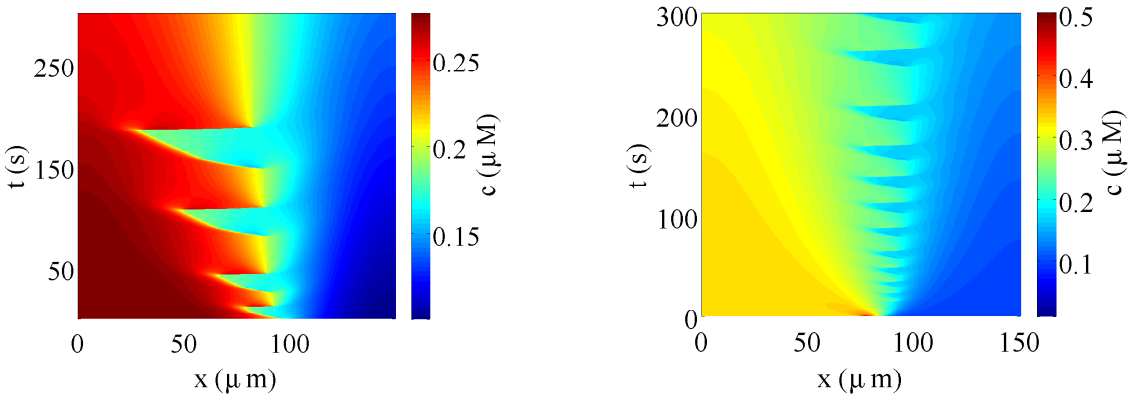

Fig. 15 Reversed tango waves for two different initial Ca^{2+} concentration profiles. The pseudocolour plot shows $c(x,t)$ in μM. Parameter values are $D = 30$ μm^{2}s^{-1}, $\tau = 0.01$ s^{-1}, $D_{\rm er} = 0.25$ μm^{2}s^{-1}, $\tau_{\rm er} = 0.5$ s^{-1}, $\bar{\eta} = 1$ s^{-1}, $\Delta = 0.5$ s, $\gamma = 0.167$, $c_{\rm th} = 0.2$ μM, and $c_T^\infty = 0.9382$ μM.

zero. In this case the tango wave front is more compact, the amplitude of the back-and-forth movement is much smaller, and no pulses are released.

Figure 15 illustrates that tango waves possess a larger variety of forms than already suggested by Figure 14. Although moving in the reverse direction, the shape of the moving edge in Figure 15 (left) is similar to the one in Figure 14 (left). A comparison between the two panels in Figure 15 reveals that the wave front is moving in opposite directions, that is, the state of low [Ca^{2+}] will eventually occupy the whole space in Figure 15 (left), while the same is true for the state of elevated [Ca^{2+}] in Figure 15 (right). Both simulations are based on the same parameter values, but on different initial conditions.

All initial conditions were set up using the same protocol. We first prepared piecewise constant concentration profiles in the cytosol and the lumen, respectively. In one part, the cytosolic and the lumenal Ca^{2+} concentrations were determined by c_T^∞ through $c^\infty = c_T^\infty/(1+\gamma\tau_{\rm er}/\tau)$ and $c_{\rm er}^\infty = c^\infty\tau_{\rm er}/\tau$. In the other part, we chose a cytosolic Ca^{2+} concentration above threshold and put the lumenal concentration to a multiple of the of $c_{\rm er}^\infty$. Then, we increased the concentration step in the ER even further by adding or subtracting appropriately chosen exponentials in the high concentration part and low concentration part, respectively. The decay constants of these exponentials were such that the contribution was restricted around the initial step. Different initial conditions varied in the extent and the size of the gap between cytosolic and ER calcium concentration levels.

5 Summary and Discussion

We have presented and analyzed a bidomain FDF model that extends the formalism introduced in (49; 50; 51; 52) to include the effect of shunting Ca^{2+} release and depletion of ER $[Ca^{2+}]$. Although the mathematical analysis is more complicated than in the single domain case, modelling Ca^{2+} release as a threshold process allows the explicit construction of travelling wave solutions in the single domain model with shunt (Section 3) as well as the full bidomain FDF model (Section 4). To our knowledge this is first demonstration that the threshold-release formalism can be applied to analyze propagating Ca^{2+} waves in a bidomain context.

For the single domain FDF model with shunt, our analytical results indicate that the propagation velocity of stable solitary pulses mediated by square pulse release is a decreasing function of the cytosolic threshold for Ca^{2+} release ($c_{\rm th}$) and an increasing function of the luminal $[Ca^{2+}]$ ($c_{\rm er}$) (Figure 1). For fixed $c_{\rm th}$ and $c_{\rm er}$, we found that the minimum stable wave speed decreases as the release rate $\overline{\eta}$ decreases even when release duration Δ is increased to maintain fixed cumulative release $\Delta\overline{\eta}$ (Figure 2). Linear stability analysis of the single domain FDF model with shunt shows that when multiple travelling pulse solutions coexist, the faster wave is stable while the slower wave is unstable (Section 3.3).

In the case of the full bidomain FDF model, we found that the propagation velocity of stable solitary pulses mediated by square pulse release is an increasing function of the total $[Ca^{2+}]$ (c_T^∞). For fixed background cytosolic $[Ca^{2+}]$ (c^∞), the requirement that the cytosolic and ER $[Ca^{2+}]$ be in equilibrium in the spatial region being invaded by the wave means that this total $[Ca^{2+}]$ is proportional to the ER $[Ca^{2+}]$; thus, the observation of Figure 7 (left) is simply that the propagation velocity of stable waves in the bidomain model increases with increasing ER $[Ca^{2+}]$. Linear stability analysis of the bidomain FDF model shows that when multiple travelling pulse solutions coexist, the faster wave is stable while the slower wave is unstable and, furthermore, the faster stable waves have larger pulse width (Figure 8). In the case of travelling fronts in the bidomain FDF model we found that the propagation velocity of stable solitary fronts mediated by step release is an increasing function of the total $[Ca^{2+}]$ (c_T^∞) (Figure 10). As presented in Section 4.5, we were also able to construct standing front solutions in the bidomain FDF model with step release.

Interestingly, the linear stability analysis of the bidomain FDF model presented in Section 4.6 shows both saddle-node (Figure 12) and dynamic (Figure 13) instabilities (on the fast branch of travelling wave solutions), the latter of which we identify with the emergence of so called tango waves that propagate in a back-and-forth manner. The presence of tango waves was confirmed in numerical simulations (Figures 14 and 15).

While the threshold-release framework is somewhat more idealized than the more conventional approach to modelling Ca^{2+} release by including gating variables for the activation and inactivation of intracellular Ca^{2+} channels, the FDF scheme has some advantages. For example, the stability analysis presented in Section 4.6 explains that the emergence of tango waves does not require any assumptions about the relative size of the cytosolic and ER Ca^{2+} diffusion coefficients, nor does this analysis assume that the basic wave which tango waves bifurcate from is stationary (cf. (40; 43; 58; 59)). It is also important to point out that some previous bifurcation analysis of stationary pulses that is relevant to bidomain models exhibiting tango waves has been possible only by prescribing a spatially inhomogeneous forcing term or a spatial variation of model parameters (43; 58; 59). Notably, the tango waves presented here do not involve spatially inhomogenous model parameters and, furthermore, the linear stability analysis presented in Section 4.6 that explains the emergence of tango waves does so by determining the spatial profiles of cytosolic and ER $[Ca^{2+}]$ self-consistently. This allows us to make a quantitative connection between bifurcation parameter sets in our analytical work and in numerical simulation.

In the bidomain FDF model we observed an increase in the luminal $[Ca^{2+}]$ at the leading edge of the wave front which extends as far as the increase in the cytosolic $[Ca^{2+}]$ that triggers release (Figure 9), in spite of the

fact that the ER diffusion coefficient was 6 times smaller than the cytolic diffusion coefficient ($D_{\rm er} = 5\ \mu{\rm m}^2{\rm s}^{-1}$ and $D = 30\ \mu{\rm m}^2{\rm s}^{-1}$, respectively). This observation suggests that the bidomain FDF formalism could be extended to include a threshold for Ca^{2+} release ($c_{\rm th}$) that is a function of the ER [Ca^{2+}] (c_{er}) and used to analyze the consequences of luminal regulation of Ca^{2+} release on the properties of Ca^{2+} waves (60). In particular, a bidomain FDF model that includes luminal regulation of Ca^{2+} release threshold might give insight into when (if ever) the traditional concept of Ca^{2+} wave propagation—waves driven by Ca^{2+}-induced Ca^{2+} release at the cytosolic wave front—must be augmented with the idea of 'sensitisation wave fronts' in which Ca^{2+} uptake via pumps at the leading edge of a wave and luminal Ca^{2+} diffusion results in Ca^{2+} release mediated by sensitization of intracellular channels to cytosolic Ca^{2+} (61). This is an area of ongoing research and will be reported upon elsewhere.

Appendix

Here we present the details of the stability analysis used in Section 4.6. Proceeding along the same lines as in Section 3.3 we express the cytosolic and the lumenal Ca^{2+} concentration profiles as

$$\begin{bmatrix} c(x,t) \\ c_{\rm er}(x,t) \end{bmatrix} = \int_{-\infty}^{t} {\rm d}s \int_{-\infty}^{\infty} {\rm d}y G(x-y,t-s) \begin{bmatrix} 1 \\ -1/\gamma \end{bmatrix} \eta(s-T(y))(c_{\rm er}(y,s)-c(y,s))\,, \tag{66}$$

where $G(x,t)$ is now a 2×2 matrix with components $G_{ij}(x,t)$, $i,j=1,2$, that correspond to the Green's function of the matrix operator

$$\mathcal{L} = \begin{bmatrix} \partial_t - D\partial_{xx} + 1/\tau & -1/\tau_{\rm er} \\ -1/(\gamma\tau) & \partial_t - D_{\rm er}\partial_{xx} + 1/(\gamma\tau_{\rm er}) \end{bmatrix}. \tag{67}$$

The matrix Green's function $G(x,t)$ can be written as an inverse Fourier transform:

$$G(x,t) = \int_{-\infty}^{\infty} \frac{{\rm d}k}{2\pi} {\rm e}^{ikx} {\rm e}^{M(k)t}, \tag{68}$$

where

$$M(k) = \begin{bmatrix} -Dk^2 - 1/\tau & 1/\tau_{\rm er} \\ 1/(\gamma\tau) & -D_{\rm er}k^2 - 1/(\gamma\tau_{\rm er}) \end{bmatrix}. \tag{69}$$

After diagonalising $M(k)$, $G(x,t)$ takes the computationally useful form

$$G(x,t) = \int_{-\infty}^{\infty} \frac{{\rm d}k}{2\pi} {\rm e}^{ikx} P(k) {\rm e}^{\Lambda(k)t} P^{-1}(k)\,. \tag{70}$$

Introducing $\sigma(k) = \tau^{-1} + Dk^2$ and $\sigma_{\rm er}(k) = (\gamma\tau_{\rm er})^{-1} + D_{\rm er}k^2$, the eigenvalues of $M(k)$ are given by

$$\lambda_{\pm}(k) = -\frac{1}{2}\left\{ \sigma(k) + \sigma_{\rm er}(k) \pm \sqrt{(\sigma(k)-\sigma_{\rm er}(k))^2 + 4/(\gamma\tau\tau_{\rm er})} \right\}, \tag{71}$$

so that

$$\Lambda(k) = \begin{bmatrix} \lambda_+(k) & 0 \\ 0 & \lambda_-(k) \end{bmatrix}, \tag{72}$$

and

$$P(k) = \begin{bmatrix} 1 & 1 \\ \tau_{\rm er}[\sigma(k)+\lambda_+(k)] & (\tau\gamma[\sigma_{\rm er}(k)+\lambda_-(k)])^{-1} \end{bmatrix}, \tag{73}$$

holds the eigenvectors of $M(k)$. Performing a linear stability analysis of (66) around a travelling wave solution in an identical fashion to that of Section 3.3 we find

$$\int_{-\infty}^{x/v} {\rm d}s \int_{-\infty}^{\infty} {\rm d}y [G_{11}(x-y,x/v-s) - \gamma^{-1}G_{12}(x-y,x/v-s)] I'(s-y/v)[g(x)-g(y)] = 0\,, \tag{74}$$

with $I(\xi) = (c_{\rm er}(v\xi) - c(v\xi))\eta(\xi)$. Hence, for the full bidomain model the characteristic equation for stability is given by (32) and (33) under the replacement of $I(\xi)$ by $(c_{\rm er}(v\xi) - c(v\xi))\eta(\xi)$, and $G(x,t)$ by $G_{11}(x,t) - \gamma^{-1}G_{12}(x,t)$.

References

1. M.J. Berridge. Inositol trisphosphate and calcium signalling. *Nature*, 361(6410):315–25, 1993.
2. M. Whitaker. Calcium at fertilization and in early development. *Physiol Rev*, 86(1):25–88, 2006.
3. S. Miyazaki and M. Ito. Calcium signals for egg activation in mammals. *J Pharmacol Sci*, 100(5):545–52, 2006.
4. D.M. Bers. Cardiac excitation-contraction coupling. *Nature*, 415(6868):198–205, 2002.
5. D.E. Clapham. Calcium signaling. *Cell*, 80(2):259–68, 1995.
6. J. Keizer, Y.X. Li, S. Stojilkovic, and J. Rinzel. InsP3-induced Ca^{2+} excitability of the endoplasmic reticulum. *Mol Biol Cell*, 6(8):945–51, 1995.
7. A. Ghosh and M.E. Greenberg. Calcium signaling in neurons: molecular mechanisms and cellular consequences. *Science*, 268(5208):239–47, 1995.
8. M.J. Berridge. Elementary and global aspects of calcium signalling. *J Physiol*, 499 (Pt 2):291–306, 1997.
9. M.J. Berridge. Neuronal calcium signaling. *Neuron*, 21(1):13–26, 1998.
10. I. Bezprozvanny and B.E. Ehrlich. The inositol 1,4,5-trisphosphate (InsP3) receptor. *J Membr Biol*, 145(3):205–16, 1995.
11. B.E. Ehrlich. Functional properties of intracellular calcium-release channels. *Curr Opin Neurobiol*, 5(3):304–9, 1995.
12. Y.X. Li, J. Keizer, S.S. Stojilkovic, and J. Rinzel. Ca^{2+} excitability of the ER membrane: an explanation for IP3-induced Ca^{2+} oscillations. *Am J Physiol*, 269(5 Pt 1):C1079–92, 1995.
13. J.D. Lechleiter and D.E. Clapham. Molecular mechanisms of intracellular calcium excitability in X. laevis oocytes. *Cell*, 69(2):283–94, 1992.
14. E.B. Ridgway, J.C. Gilkey, and L.F. Jaffe. Free calcium increases explosively in activating medaka eggs. *Proc Natl Acad Sci U S A*, 74(2):623–7, 1977.
15. R Nuccitelli, D L Yim, and T Smart. The sperm- induced Ca^{2+} wave following fertilization of the Xenopus eggs requires the production of Ins(1,4,5)P3. *Developmental Biology*, 158:200–212, 1993.
16. S.A. Stricker, V.E. Centonze, and R.F. Melendez. Calcium dynamics during starfish oocyte maturation and fertilization. *Dev Biol*, 166(1):34–58, 1994.
17. R. Dumollard, A. McDougall, C. Rouvire, and C. Sardet. Fertilisation calcium signals in the ascidian egg. *Biol Cell*, 96(1):29–36, 2004.
18. H. Cheng, M.R. Lederer, W.J. Lederer, and M.B. Cannell. Calcium sparks and $[Ca^{2+}]_i$ waves in cardiac myocytes. *Am J Physiol*, 270(1):C148–59, 1996.
19. C.H. Lee, D. Poburko, K.H. Kuo, C.Y. Seow, and C. van Breemen. Ca^{2+} oscillations, gradients, and homeostasis in vascular smooth muscle. *Am J Physiol Heart Circ Physiol*, 282(5):H1571–83, 2002.
20. X. Ying, Y. Minamiya, C. Fu, and J. Bhattacharya. Ca^{2+} waves in lung capillary endothelium. *Circ Res*, 79(4):898–908, 1996.
21. C.C. Fink, B. Slepchenko, I.I. Moraru, J. Watras, J.C. Schaff, and L.M. Loew. An image-based model of calcium waves in differentiated neuroblastoma cells. *Biophys J*, 79(1):163–83, 2000.
22. T.A. Fiacco and K.D. McCarthy. Astrocyte calcium elevations: properties, propagation, and effects on brain signaling. *Glia*, 54(7):676–90, 2006.
23. K. Kiselyov, X. Wang, D.M. Shin, W. Zang, and S. Muallem. Calcium signaling complexes in microdomains of polarized secretory cells. *Cell Calcium*, 40(5-6):451–9, 2006.

24. G. Dupont and A. Goldbeter. Oscillations and waves of cytosolic calcium: insights from theoretical models. *Bioessays*, 14(7):485–93, 1992.
25. A. Atri, J. Amundson, D. Clapham, and J. Sneyd. A single-pool model for intracellular calcium oscillations and waves in the Xenopus laevis oocyte. *Biophys J*, 65(4):1727–39, 1993.
26. J. Sneyd, S. Girard, and D. Clapham. Calcium wave propagation by calcium-induced calcium release: an unusual excitable system. *Bull Math Biol*, 55(2):315–44, 1993.
27. G. Dupont and A. Goldbeter. Properties of intracellular Ca^{2+} waves generated by a model based on Ca^{2+}-induced Ca^{2+} release. *Biophys J*, 67(6):2191–204, 1994.
28. M.S. Jafri and J. Keizer. Diffusion of inositol 1,4,5-trisphosphate but not Ca^{2+} is necessary for a class of inositol 1,4,5-trisphosphate-induced Ca^{2+} waves. *Proc Natl Acad Sci U S A*, 91(20):9485–9, 1994.
29. M.S. Jafri and J. Keizer. On the roles of Ca^{2+} diffusion, Ca^{2+} buffers, and the endoplasmic reticulum in IP3-induced Ca^{2+} waves. *Biophys J*, 69(5):2139–53, 1995.
30. M.S. Jafri and J. Keizer. Agonist-induced calcium waves in oscillatory cells: a biological example of burgers' equation. *Bull Math Biol*, 59(6):1125–44, 1997.
31. J. Wagner, Y.X. Li, J. Pearson, and J. Keizer. Simulation of the fertilization Ca^{2+} wave in Xenopus laevis eggs. *Biophys J*, 75(4):2088–97, 1998.
32. J Sneyd. *An introduction to Mathematical Modeling in Physiology, Cell Biology, and Immunology*, chapter Calcium excitability, pages 83–118. American Mathematical Society, 2002.
33. C.P. Fall, J.M. Wagner, L.M. Loew, and R. Nuccitelli. Cortically restricted production of IP3 leads to propagation of the fertilization Ca^{2+} wave along the cell surface in a model of the Xenopus egg. *J Theor Biol*, 231(4):487–96, 2004.
34. M. Falcke, Y. Li, J.D. Lechleiter, and P. Camacho. Modeling the dependence of the period of intracellular Ca^{2+} waves on SERCA expression. *Biophys.J.*, 85:1474–1481, 2003.
35. G W De Young and J Keizer. A single pool IP_3-receptor based model for agonist stimulated Ca^{2+} oscillations. *Proceedings of the National Academy of Sciences USA*, 89:9895–9899, 1992.
36. Y.X. Li and J. Rinzel. Equations for InsP3 receptor-mediated $[Ca^{2+}]_i$ oscillations derived from a detailed kinetic model: a Hodgkin-Huxley like formalism. *J Theor Biol*, 166(4):461–73, 1994.
37. J Keener and J Sneyd. *Mathematical Physiology*. Springer, 1998.
38. G.D. Smith, J.E. Pearson, and J.E. Keizer. Modeling intracellular Ca^{2+} waves and sparks. In C.P. Fall, E.S. Marland, J.M. Wagner, and J.J. Tyson, editors, *Computational Cell Biology, Fall CP et al., eds*, pages 198–229. Springer-Verlag, 2002.
39. J. Sneyd, J. Keizer, and M.J. Sanderson. Mechanisms of calcium oscillations and waves: a quantitative analysis. *FASEB J*, 9(14):1463–72, 1995.
40. Y-X Li. Tango waves in a bidomain model of fertilization calcium waves. *Physica D*, 186:27–49, 2003.
41. S A Stricker. Repetitive calcium waves induced by fertilization in the nemertean worm *Cerebratulus lacteus*. *Developmental Biology*, 176:243–263, 1996.
42. M Yoshida, N Sensui, T Inoue, M Morisawa, and K Mikoshiba. Role of two series of Ca^{2+} oscillations in activation of ascidian eggs. *Developmental Biology*, 203:122–133, 1998.
43. A Prat and Y-X Li. Stability of front solutions in inhomogeneous media. *Physica D*, 186:50–68, 2003.
44. Y. Yao, J. Choi, and I. Parker. Quantal puffs of intracellular Ca^{2+} evoked by inositol trisphosphate in Xenopus oocytes. *J Physiol*, 482:533–553, 1995.
45. I. Parker, J. Choi, and Y. Yao. Elementary events of InsP3-induced Ca^{2+} liberation in Xenopus oocytes: hot spots, puffs and blips. *Cell Calcium*, 20(2):105–21, 1996.
46. A.E. Bugrim, A.M. Zhabotinsky, and I.R. Epstein. Calcium waves in a model with a random spatially discrete distribution of Ca^{2+} release sites. *Biophys J*, 73(6):2897–906, 1997.

47. H. Cheng, W.J. Lederer, and M.B. Cannell. Calcium sparks: elementary events underlying excitation-contraction coupling in heart muscle. *Science*, 262(5134):740–4, 1993.
48. J E Keizer and G D Smith. Spark-to-wave transition: saltatory transmission of calcium waves in cardiac myocytes. *Biophysical Chemistry*, 72:87–100, 1998.
49. J. Keizer, G.D. Smith, S. Ponce-Dawson, and J.E. Pearson. Saltatory propagation of Ca^{2+} waves by Ca^{2+} sparks. *Biophys J*, 75(2):595–600, 1998.
50. J E Pearson and S Ponce Dawson. Crisis on skid row. *Physica A*, 257:141–148, 1998.
51. S P Dawson, J Keizer, and J E Pearson. Fire-diffuse-fire model of dynamics of intracellular calcium waves. *Proceedings of the National Academy of Sciences USA*, 96:6060–6063, 1999.
52. S Coombes. The effect of ion pumps on the speed of travelling waves in the fire-diffuse-fire model of Ca^{2+} release. *Bulletin of Mathematical Biology*, 63:1–20, 2001.
53. S Coombes and Y Timofeeva. Sparks and waves in a stochastic fire-diffuse-fire model of Ca^{2+} release. *Physical Review E*, 68:021915, 2003.
54. S Coombes, R Hinch, and Y Timofeeva. Receptors, sparks and waves in a fire-diffuse-fire framework for calcium release. *Progress in Biophysics and Molecular Biology*, 85:197–216, 2004.
55. Y. Timofeeva and S. Coombes. Directed percolation in a two-dimensional stochastic fire-diffuse-fire model. *Phys Rev E Stat Nonlin Soft Matter Phys*, 70(6 Pt 1):062901, 2004.
56. Y Timofeeva and S Coombes. Wave bifurcation and propagation failure in a model of calcium release. *Journal of Mathematical Biology*, 47:249–269, 2003.
57. T R Shannon, F Wang, J Puglisi, C Weber, and D M Bers. A mathematical treatment of integrated Ca dynamics within the ventricular myocyte. *Biophysical Journal*, 87:3351–3371, 2004.
58. P.C. Bressloff, S.E. Folias, A. Prat, and Y.X. Li. Oscillatory waves in inhomogeneous neural media. *Phys Rev Lett*, 91(17):178101, 2003.
59. A. Prat, Y.X. Li, and P. Bressloff. Inhomogeneity-induced bifurcation of stationary and oscillatory pulses. *Physica D*, 202:177–99, 2005.
60. D Terentyev, S Viatchenko-Karpinski, H H Valdivia, A L Escobar, and S Gyorke. Luminal Ca controls termination and refractory behaviour of Ca induced Ca release in cardiac myocytes. *Cirulatory Research*, 91:414–420, 2002.
61. M. Keller, J.P. Kao, M. Egger, and E. Niggli. Calcium waves driven by "sensitization" wave-fronts. *Cardiovascular Research*, 74(1):39–45, 2007.